

## The soft-photon approximation in infrared-laser-assisted atomic ionization by extreme-ultraviolet attosecond-pulse trains

Álvaro Jiménez Galán<sup>1</sup>, Luca Argenti<sup>1,3</sup> and Fernando Martín<sup>1,2</sup>

<sup>1</sup> Departamento de Química, Módulo 13, Universidad Autónoma de Madrid, E-28049 Madrid, Spain, EU

<sup>2</sup> Instituto Madrileño de Estudios Avanzados en Nanociencia (IMDEA-Nanociencia), Cantoblanco, E-28049 Madrid, Spain, EU  
E-mail: [luca.argenti@uam.es](mailto:luca.argenti@uam.es)

*New Journal of Physics* **15** (2013) 113009 (28pp)

Received 27 May 2013

Published 7 November 2013

Online at <http://www.njp.org/>

doi:10.1088/1367-2630/15/11/113009

**Abstract.** We use the soft-photon approximation, formulated for finite pulses, to investigate the effects of the dressing pulse duration and intensity on simulated attosecond pump–probe experiments employing trains of attosecond extreme-ultraviolet pulses in conjunction with an IR probe pulse. We illustrate the validity of the approximation by comparing the modelled photoelectron distributions for the helium atom, in the photon energy region close to the  $N = 2$  threshold, to the results from the direct solution of the time-dependent Schrödinger equation for two active electrons. Even in the presence of autoionizing states, the model accurately reproduces most of the background features of the *ab initio* photoelectron spectrum in the 1s channel. A splitting of the photoelectron harmonic signal along the polarization axis, in particular, is attributed to the finite duration of the probe pulse. Furthermore, we study the dependence of the sideband integrated signal on the pump–probe time delay for increasing IR field strengths. Starting at IR intensities of the order of  $\sim 1 \text{ TW cm}^{-2}$ , overtones in the sideband oscillations due to the exchange of three or more IR photons start to appear. We derive an analytical expression in the frequency-comb limit of the

<sup>3</sup> Author to whom any correspondence should be addressed.



Content from this work may be used under the terms of the [Creative Commons Attribution 3.0 licence](https://creativecommons.org/licenses/by/3.0/). Any further distribution of this work must maintain attribution to the author(s) and the title of the work, journal citation and DOI.

soft-photon model for the amplitude of all the sideband frequency components and show that these amplitudes oscillate as a function of the intensity of the IR field. In particular, we predict that the amplitude of the fundamental component with frequency  $2\omega_{\text{IR}}$ , on which the RABITT optical reconstruction technique is based, changes sign periodically.

## Contents

<b>1. Introduction</b>	<b>2</b>
<b>2. The soft-photon approximation</b>	<b>5</b>
2.1. Monochromatic soft-photon approximation . . . . .	7
2.2. Pulsed soft-photon approximation . . . . .	9
2.3. Frequency-comb limit . . . . .	10
<b>3. Results</b>	<b>13</b>
3.1. Single attosecond pulse case . . . . .	13
3.2. Attosecond pulse train case: effect of finite probe duration . . . . .	16
3.3. Attosecond pulse train case: effect of high probe intensity . . . . .	17
<b>4. Conclusions</b>	<b>21</b>
<b>Acknowledgments</b>	<b>21</b>
<b>Appendix A. Perturbative RABITT amplitude</b>	<b>21</b>
<b>Appendix B. <i>Ab initio</i> calculation of photoelectron spectra</b>	<b>23</b>
<b>References</b>	<b>25</b>

## 1. Introduction

Recent major advances in laser technology have led to the production of single attosecond pulses (SAP) [1, 2] as well as attosecond pulse trains (APT) [3, 4] in the extreme-ultraviolet (XUV) energy range, thus opening the way to the experimental study of electron dynamics in atoms and molecules at its natural timescale [5]. Owing to the still comparatively low intensity of the sub-femtosecond XUV pulses [6] obtained with high-harmonic generation (HHG) [7–9], table-top experiments that investigate such ultra-fast dynamics generally involve pump–probe schemes comprising a sequence of one or more XUV pulses in conjunction with a replica of the intense compressed Ti–sapphire infrared (IR) pulse used to create them [10–12]. As a result of the interaction with the field, an atomic or molecular target is ionized and the fragments emerging from the reaction centre are collected (the recent technique of attosecond transient absorption spectroscopy represents a notable exception [13]). The spectral and angular distribution of the photo fragments encode information about all the steps of the process triggered by light: the initial excitation out of the original bound state, the field-free evolution of coherent superpositions of states in the continuum during the timegap between pump and probe pulse, the dressed-state dynamics within the IR field as well as further transitions between excited states induced by the probe. Disentangling the contribution of these steps from the experimental result is a hard task which often requires assistance by theory. Indeed, since non-stationary non-perturbative transitions between highly excited states may be involved, direct solution of the time-dependent Schrödinger equation (TDSE) is often needed to reproduce the experiment in all its aspects and in a quantitative way. Freezing of selected degrees of freedom in the system,

fine tuning of the laser parameters and wave-packet inspection can be used to characterize the underlying ionization mechanism. Yet, this is a time-consuming procedure. The analysis of both experiments and theoretical simulations is thus greatly facilitated if major aspects of the results can be explained by simplified models. In the case of atomic photoionization, a most prominent example is the strong-field approximation [14–16], a model which is able to reproduce well broad features of the photoelectron spectrum and which provided a valuable insight into several non-perturbative processes triggered by radiation (see, e.g. [17, 18] and references therein).

In the context of laser-assisted photoelectric effect, applications of the strong-field approximation have concentrated on the description of sideband intensities for long single XUV pulses [19–21] and on the transition to the streaking regime [22–24] when the XUV pulse duration is reduced below one femtosecond [25–28]. A reconstruction method for SAPs based on the strong field approximation and on measurements conducted at different intensities of the dressing laser has also been proposed [29]. Since in all these cases, the energy of the photoelectron is much larger than that of a single quantum of the dressing field, the more specialized term soft-photon approximation (SPA) [20] will be used.

In this work, we examine in some detail the use of the SPA to reproduce the outcome of a second important class of attosecond pump–probe schemes, those employing an APT in conjunction with an IR pulse with a controllable time delay, which is the laser configuration also used for the popular reconstruction of attosecond beating by interference of two-photon transitions technique (RABITT) [3, 19, 30]. In particular, we investigate the role of probe pulse duration and intensity on the photoelectron distribution. To justify the general validity of our results, we compare the prediction of the SPA, formulated for finite pump pulses and modulated dressing fields, for the photoionization of the helium atom, the simplest system which features correlated electron dynamics, with the virtually exact *ab initio* results obtained by numerical integration of the TDSE on a multi-channel *B*-spline close-coupling basis [31]. This is a particularly stringent and relevant test since, so far, the applicability of the SPA has been validated mostly by comparison with single-active electron models only. The results of our calculations show that, even at the opening of the  $N = 2$  excitation threshold of the  $\text{He}^+$  parent ion, an energy region where electronic correlation is known to play a crucial role, the SPA reproduces with high accuracy all of the most prominent background non-resonant features of the spectrum in the  $1s$  dominant ionization channel. For example, simulations with compressed Ti-sapphire pulses reveal unexpected minima in the harmonic photoelectron signal along the polarization axis. These minima are accurately reproduced by an extension of the SPA model where the pulsed nature of the dressing field is mimicked by a periodic envelope, hence they are shown to be associated with the finite duration of the IR pulse, rather than to the underlying atomic structure. In other terms, not only can the SPA describe several aspects of atomic attosecond photoionization spectra but also proves useful to tell apart those non-perturbative aspects of the ionization process that can be explained by a single-particle model from those with genuine many-body character.

Based on the good agreement between SPA and the *ab initio* calculations in selected cases, we examined the prediction of the model for APT-pump IR-probe experiments at increasingly large intensities of the dressing laser. This line of investigation is relevant both to highlight how the photoelectron spectrum deviates from the weak-field limit assumed in the RABITT technique, and to lay out the ground for an extension of interferometric methods like RABITT to study strong-field effects. The RABITT technique was originally introduced to characterize the

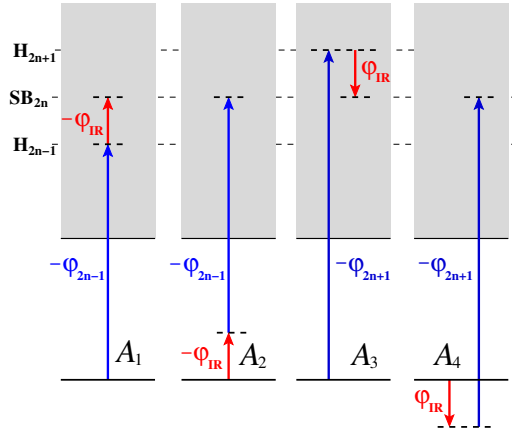


**Figure 1.** The four lowest-order two-photon transition amplitudes that give rise to the sideband  $2n$  in the RABITT scheme. Since both the absorption and stimulated emission of one photon carry the phase of the corresponding field, but with opposite signs, interference terms of the form  $\mathcal{A}_{1,2}^* \mathcal{A}_{3,4} + \text{c.c.}$  oscillate as  $2\varphi_{IR} = 2\omega_{IR}t_d$ , where  $t_d$  is the time delay between the IR pulse and the APT.

average temporal profile of the attosecond pulses within the train [32–35] and, in turn, devise manipulation techniques to minimize the duration of individual pulses [36, 37]. This procedure is based on two assumptions: that the transition matrix elements between atomic states in the continuum vary slowly with the photoelectron energy, and that the probe pulse is sufficiently weak for the lowest-order perturbative approximation to apply. The spectrum of the APT used in the RABITT method comprises only odd harmonics ( $H_{2n+1}$ ) of the IR frequency. At low IR intensities, the absorption of one XUV photon combined with the exchange of one IR photon gives rise to sidebands ( $SB_{2n}$ ) in the photoelectron spectrum corresponding to even multiples of the IR photon energy (see figure 1). Owing to the interference between the amplitudes for the absorption of two consecutive harmonics,  $H_{2n-1}$  and  $H_{2n+1}$ , the intensity of the sideband  $SB_{2n}$  oscillates as a function of the time delay between the XUV train and the IR pulse at twice the frequency of the IR. The perturbative expression for the two-photon transition rate  $\mathcal{W}_{2n}^{(2)}$  to the sideband  $SB_{2n}$  is

$$\mathcal{W}_{2n}^{(2)} = \frac{8\pi^3}{\omega_{IR}} \Phi_{IR} \left\{ \Phi_{2n-1} |\mathcal{M}_{2n-1}|^2 + \Phi_{2n+1} |\mathcal{M}_{2n+1}|^2 + 2\sqrt{\Phi_{2n-1}\Phi_{2n+1}} |\mathcal{M}_{2n-1}\mathcal{M}_{2n+1}| \cos [\Delta\phi_{2n} + \Delta\varphi_{2n}^{\text{At}} - 2(\varphi_{IR,0} + \omega_{IR}t_d)] \right\}, \quad (1.1)$$

where  $\mathcal{M}_{2n\pm1}$  are two-photon transition matrix elements,  $\Phi_{IR}$  and  $\Phi_{2n\pm1}$  are the IR and the harmonic photon fluxes,  $\Delta\phi_{2n}$  is the phase difference between the  $H_{n+1}$  and  $H_{n-1}$  harmonics and  $\omega_{IR}$  and  $\varphi_{IR,0}$  are the IR angular frequency and absolute phase, respectively,  $t_d$  is the pump–probe time delay and  $\Delta\varphi_{2n}^{\text{At}}$  is a so-called atomic phase (see appendix A for the definition of the individual terms and an outline of the derivation of (1.1)). Hence, the phase of the oscillation incorporates the intrinsic phases of all the atomic transitions involved as well as the relative phases of the harmonics in the XUV train.

With the increase of the APT reproducibility and control, interest has shifted from the characterization of light pulses to the measurement of intrinsic phases  $\Delta\varphi^{\text{At}}$ , which

provide access to the time delay in photoelectron ejection [38–40] and to resonant continuum–continuum transition in atoms [41] and molecules [42, 43]. The RABITT technique, therefore, constitutes a valid alternative to the measurement of photoelectron ejection time delays based on the streaking technique [11, 44–51]. APTs were also used, in association with strong driving fields, to demonstrate control of the ionization rate [52–54] and, in the presence of both even and odd harmonics, to alter photoelectron anisotropy [55].

From the perspective of devising effective quantum-control protocols, it is interesting to examine extensions of the RABITT technique beyond the lowest-order perturbative limit. At higher intensities, more than one IR photon can be exchanged. When this happens, overtones appear in the sideband modulation with time delay; consequently, the direct correspondence between each sideband phase and the phase differences between consecutive harmonics is lost. To quantify the effects of strong fields on sidebands, we derive a general analytical expression for the dependence of the overtone intensity on the dressing-field strength in the frequency-comb limit. Qualitative departure from the lowest-order perturbative regime is predicted already at intensities as low as  $5 \times 10^{11} \text{ W cm}^{-2}$ , where multi-photon contributions start to dominate. In fact, we show that the amplitudes of all the frequency components in a sideband oscillate as a function of the intensity of the IR field. In particular, we predict that the amplitude of the dominant RABITT component should periodically change sign. Both the aforementioned effect due to a finite dressing pulse duration and the one predicted for large IR intensities should realistically be observable with the currently available experimental setups.

The paper is organized as follows. In section 2 we shortly survey the SPA formulated for finite XUV pulses, extend it to the case of a modulated IR, apply it to the RABITT pump–probe scheme and derive an expression for the sideband intensities in the limiting case of an XUV frequency comb. In section 3 we illustrate the results obtained within the modified SPA and compare them with the results from virtually exact *ab initio* simulations, in the specific case of helium ionization, and with the frequency comb model for a general case in the high-intensity regime. In section 4, we summarize our results and present our conclusions. The paper is closed by an appendix section: in appendix A we offer a concise derivation of the lowest-order perturbative RABITT formula; in appendix B we outline the procedure followed to compute the *ab initio* solution of the TDSE and the value of the corresponding asymptotic differential observables.

## 2. The soft-photon approximation

Consider an atom  $A$  in its ground state  $|\phi_g\rangle$  subject to a strong IR pulse and a weak XUV pulse (or pulse train) triggering the ionization process

$$A + \gamma_{\text{XUV}} \pm n\gamma_{\text{IR}} \rightarrow A^+ + e_{\vec{k}}^-, \quad (2.1)$$

where  $\vec{k}$  is the momentum of the ejected photoelectron. The evolution of the system is described by the minimal coupling time-dependent Hamiltonian which, in dipole approximation and in velocity gauge [56], reads

$$H(t) = H_0 + \alpha[\vec{A}_{\text{IR}}(t) + \vec{A}_{\text{XUV}}(t)] \cdot \vec{P}, \quad (2.2)$$

where  $H_0$  is the field-free time-independent atomic potential,  $\alpha$  is the fine-structure constant,  $\vec{A}_{\text{XUV}}(t)$  and  $\vec{A}_{\text{IR}}$  are the transverse vector potentials of the XUV and IR pulses, respectively,

and  $\vec{P}$  is the total electronic canonical momentum (atomic units are used throughout, unless otherwise stated).

Since the XUV field is assumed to be weak, its effects can be treated at the level of the first-order time-dependent perturbation theory. If the intensity of the IR field is to take on large values, however, the interaction of the atom with it must be treated non-perturbatively. Therefore, the transition amplitude  $\mathcal{A}_{\lambda \leftarrow g}$  from the initial state  $|\phi_g\rangle$  to a final scattering state  $|\phi_\lambda^-\rangle$  of the time-independent Hamiltonian  $H_0$  (the minus and  $\lambda$  indices in the final state stand for incoming boundary conditions and for a complete set of appropriate asymptotic quantum numbers, respectively) is given by the generalized expression

$$\mathcal{A}_{\lambda \leftarrow g} = -i \int_{-\infty}^{+\infty} \langle \psi_\lambda^-(t) | \alpha \vec{A}_{\text{XUV}}(t) \cdot \vec{P} | \psi_g^+(t) \rangle dt, \quad (2.3)$$

where  $|\psi_g^+(t)\rangle$  and  $|\psi_\lambda^-(t)\rangle$  are the dressed states of the time-dependent Hamiltonian

$$H_F(t) = H_0 + \alpha \vec{A}_{\text{IR}}(t) \cdot \vec{P}, \quad (2.4)$$

which fulfil the assigned asymptotic conditions at  $t \rightarrow \mp\infty$ , respectively,

$$i\partial_t |\psi_g^+\rangle = H_F(t) |\psi_g^+\rangle, \quad \lim_{t \rightarrow -\infty} e^{iE_g t} |\psi_g^+(t)\rangle = |\phi_g\rangle, \quad (2.5a)$$

$$i\partial_t |\psi_\lambda^-\rangle = H_F(t) |\psi_\lambda^-\rangle, \quad \lim_{t \rightarrow +\infty} e^{iE_\lambda t} |\psi_\lambda^-(t)\rangle = |\phi_\lambda^-\rangle, \quad (2.5b)$$

where  $E_g$  and  $E_\lambda$  are the initial and final energy, respectively.

We will now concentrate on the process of laser-assisted photoionization in the SPA, i.e. the central frequency of the XUV pulse is assumed to be sufficiently high to drive the photoelectron well above the ionization threshold so that the IR field dresses the atom, thus generating multiphoton transitions between the continuum states, but the final photoelectron spectrum still lies well above the ionization threshold and recollision is excluded. To evaluate this amplitude within the soft-photon model, we make three approximations. (I) The ground state  $|\phi_g\rangle$  is unaffected by the IR field,  $|\psi_g^+(t)\rangle = e^{-iE_g t} |\phi_g\rangle$  identically. (II) The atom behaves as an hydrogenic system which is ionized from the 1s orbital. (III) The interaction of the emitted photoelectron with the parent ion is neglected altogether. Less severe approximations which account for the interaction of the bound state with the dressing field [20], and for the interaction of the continuum state with the parent ion at a perturbative level [57, 58] have been considered in the past. These investigations confirm that if the neutral atom has large excitation energies, as it is certainly the case for helium, and the final energy of the photoelectrons are sufficiently far from the ionization threshold, these are reasonable approximations at the laser intensities realized for current compressed Ti-sapphire pulses. The choice of a hydrogenic orbital for the initial ground state, a common practice in atomic structure modelling, is particularly justified in the case of laser-assisted XUV ionization since only the high-energy components of the orbital representation in momentum space, which are the least sensitive to the electron-electron interaction, contribute to the transition amplitudes. Under the assumptions (I–III), the final state  $|\psi_\lambda^-(t)\rangle$  in (2.3) reduces to a Volkov state  $|\Psi_{\vec{k}}(t)\rangle$  [56]

$$|\Psi_{\vec{k}}(t)\rangle = |\vec{k}\rangle \exp \left[ -i \frac{k^2}{2} t - i \Theta(t) \right], \quad \Theta(t) = \alpha \vec{k} \cdot \int_0^t d\tau \vec{A}_{\text{IR}}(\tau). \quad (2.6)$$



### 2.1. Monochromatic soft-photon approximation

For a monochromatic IR field,

$$\vec{A}_{\text{IR}}(t) = A_0 \cos(\omega_{\text{IR}} t + \varphi_{\text{IR}}) \hat{\epsilon}, \quad (2.7)$$

where  $A_0$ ,  $\omega_{\text{IR}}$ ,  $\varphi_{\text{IR}}$  and  $\hat{\epsilon}$  are the field amplitude, frequency, phase and polarization, respectively. The time-dependent phase  $\Theta(t)$ , therefore, reads

$$\Theta(t) = \vec{\alpha}_0 \cdot \vec{k} \sin(\omega_{\text{IR}} t + \varphi_{\text{IR}}) - \vec{\alpha}_0 \cdot \vec{k} \sin(\varphi_{\text{IR}}), \quad (2.8)$$

where we introduced the free-electron excursion amplitude  $\vec{\alpha}_0 = \alpha \omega_{\text{IR}}^{-1} A_0 \hat{\epsilon}$ . The second term on the rhs of (2.8) results in a time-independent phase factor in the wave function, equivalent to an intensity-dependent phase convention for the plane wave basis, which disappears when taking the square module of the transition amplitudes to compute observable quantities. Therefore, in the following, we will simply neglect it. We can apply, as usual, the Jacobi–Anger expansion [59] to obtain

$$|\Psi_{\vec{k}}(t; \vec{\alpha}_0)\rangle = |\vec{k}\rangle \sum_{n=-\infty}^{\infty} J_n(\vec{\alpha}_0 \cdot \vec{k}) \exp[-i(k^2/2 + n\omega_{\text{IR}})t - in\varphi_{\text{IR}}], \quad (2.9)$$

where  $J_n$  are Bessel functions and  $|\vec{k}\rangle$  is a plane wave,  $\langle \vec{r} | \vec{k} \rangle = (2\pi)^{-3/2} \exp(i\vec{k} \cdot \vec{r})$ . If we substitute (2.9) in (2.3), we obtain

$$\mathcal{A}_{\vec{k} \leftarrow g} \cong -i\sqrt{2\pi} \alpha (\vec{k} \cdot \hat{\epsilon}) \phi_g(k) \sum_{n=-\infty}^{+\infty} J_n(\xi x) e^{in\varphi_{\text{IR}}} \tilde{A}_{\text{XUV}}(E_g - k^2/2 - n\omega_{\text{IR}}), \quad (2.10)$$

where  $\phi_g(k)$  is the momentum representation of a 1s orbital with effective charge  $Z$  [60],

$$\phi_{1s}(k) = \frac{2\sqrt{2}Z^{5/2}}{\pi[k^2 + Z^2]^2}, \quad (2.11)$$

$x$  is the cosine of the angle formed by the photoelectron momentum and the laser polarization, and where we introduced the reduced field strengths  $\xi = \alpha_0 k$ . The reduced field strength, formulated in terms of the photoelectron energy  $E_e$  and of the IR intensity  $I_{\text{IR}}$  expressed in  $\text{TW cm}^{-2}$ ,

$$\xi = \frac{4\sqrt{\pi\alpha} E_e^{1/2}}{\omega_{\text{IR}}^2} \sqrt{\frac{I_{\text{IR}}(\text{TW cm}^{-2})}{3.51 \times 10^4 \text{ TW cm}^{-2}}}, \quad (2.12)$$

is a very convenient quantity in the context of attosecond pump–probe experiments, since, for  $E_e = 1 \text{ au}$ , an intensity  $I_{\text{IR}} = 1 \text{ TW cm}^{-2}$ , a common order of magnitude for compressed Ti–sapphire pulses, corresponds to  $\xi \simeq 0.99$ , i.e. it is essentially equivalent to one reduced field strength unit. In equation (2.10) as well as in the following, the character tilda on top of a symbol indicates the Fourier transform of the corresponding time-dependent variable, e.g.

$$\tilde{A}_{\text{XUV}}(\omega) = \frac{1}{\sqrt{2\pi}} \int_{-\infty}^{+\infty} e^{-i\omega t} A_{\text{XUV}}(t) dt. \quad (2.13)$$

Equation (2.10) can be directly used to compute the photoelectron distribution as

$$\frac{dP_{E\hat{\Omega} \leftarrow g}}{dE d\Omega} = k |\mathcal{A}_{\vec{k} \leftarrow g}|^2 \quad (2.14)$$

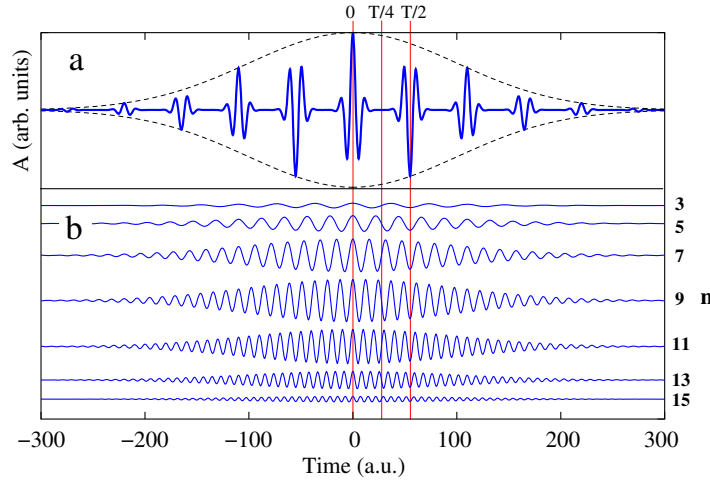


**Figure 2.** Schematic representation of an APT (a) and of its harmonic composition (b). When the harmonics are all in phase at a given point along their trajectory, they interfere constructively giving rise to a localized attosecond pulse ( $t = 0$ ). At a distance of half an IR cycle in either space ( $\Delta x = \lambda_{\text{IR}}/2$ ) or time ( $\Delta t = T_{\text{IR}}/2$ ) from this maximum, all the harmonics will be in phase again but with opposite sign, thus giving rise to a second attosecond pulse which is the mirror image of the first one with respect to the horizontal axis. At  $t = T_{\text{IR}}/4$ , all the harmonics vanish and so does the train.

and applied to several cases of interest. In section 3, we will examine a few. For monochromatic XUV pulses, further simplifications of (2.14) are possible [16, 18, 20]. Here, however, we are more interested in broadband XUV pulses in general, and on APTs in particular. First, we will specialize the formula for the transition amplitude (2.10) to the RABITT technique. Next, we will see how the case of a finite IR pulse can be simulated with a polychromatic Volkov state.

An idealized APT can be expressed as a modulated infinite sequence of identical pulses

$$A_{\text{XUV}}(t) = A_0 g(t) \sum_{n=-\infty}^{+\infty} (-1)^n f(t - n\pi/\omega_{\text{IR}}), \quad (2.15)$$

where  $g(t)$  is the envelope of the train and  $f(t)$  is the (dimensionless) profile, centred at the time origin, of each single pulse in the train. Alternatively, the same train can also be expressed as a combination of in-phase harmonics of the fundamental IR frequency (see figure 2),

$$A_{\text{XUV}}(t) = \sqrt{\frac{8}{\pi}} \omega_{\text{IR}} A_0 g(t) \sum_{k=0}^{\infty} |\tilde{f}_{2k+1}| \cos[(2k+1)\omega_{\text{IR}}t + \phi_{2k+1}], \quad (2.16)$$

where the index  $k$  runs now over the harmonics, and we introduced the notation  $\tilde{f}_n = \tilde{f}(n\omega_{\text{IR}})$ ,  $\phi_n = \arg f_n$ . The spectrum of this field thus reads

$$\tilde{A}_{\text{XUV}}(\omega) = \sqrt{\frac{2}{\pi}} A_0 \omega_{\text{IR}} \sum_{k=-\infty}^{+\infty} \tilde{f}_{2k+1} \tilde{g}[\omega - (2k+1)\omega_{\text{IR}}]. \quad (2.17)$$

In the following we will consider only the case of the in-phase harmonics. However, the formalism developed in our paper is very easily extended to include explicitly the harmonic



phases  $\phi_{2k+1}$ , and hence to devise possible corrections to the RABITT reconstruction protocol when a structureless ionization continuum is involved. To include in a consistent way the effect of the atomic phases (and of their energy derivatives, which are associated with the laser-assisted photoelectron ejection time delay), instead, one first needs a realistic model for the arguments of the multi photon transition matrix elements for a particle in a Coulomb field and in the presence of a reactive parent ion. Investigation in this direction, while certainly worth pursuing, is to be considered beyond the scope of the current work.

## 2.2. Pulsed soft-photon approximation

To the best of our knowledge, the SPA has only been used in the monochromatic IR version outlined in the previous paragraph. This approximation, however, is justified only if the envelope of this dressing pulse does not change significantly across the duration of the XUV field. This is certainly the case of SAPs, where the full-width at half-maximum (fwhm) of the XUV does not exceed a half period of the IR (streaking conditions). It is generally the case in the RABITT method as well, since common IR pulses have a duration of a few tens of femtoseconds, which is longer than the common duration of an APT. Yet, compressed IR pulses with a duration of only a few femtoseconds are routinely produced [1, 2] and it is in principle not hard to devise an experiment where an APT is aligned with a compressed replica of the IR pulse used to generate it and which could easily be as short as the APT itself. Furthermore, use of short IR pulses is common practice when solving the TDSE to limit the cost of computation, or even to render the simulation possible altogether. The IR modulation can be appropriately accounted for with a truncated cosine-square envelope

$$\vec{A}_{\text{IR}}(t) = \begin{cases} A_0 \hat{e} \cos^2[\Omega(t - t_{\text{IR}})] \cos[\omega_{\text{IR}}(t - t_{\text{IR}}) + \varphi_{\text{IR}}], & \text{for } |t - t_{\text{IR}}| < \frac{\pi}{2\Omega} \\ \vec{0} & \text{otherwise.} \end{cases} \quad (2.18)$$

Since in the SPA model we are dealing with a structureless continuum, the multi-photon transition amplitudes which involve the absorption of at least one photon from the XUV field rapidly vanish as soon as the XUV and the IR pulses do not overlap. As a consequence, to examine the influence of a finite duration of the IR dressing field, one can replace the cosine-square single IR pulse (2.18) by a cosine-square *periodic* envelope,

$$\vec{A}_{\text{IR}}(t) = A_0 \hat{e} \cos^2[\Omega(t - t_{\text{IR}})] \cos[\omega_{\text{IR}}(t - t_{\text{IR}}) + \varphi_{\text{IR}}] \quad \forall t, \quad (2.19)$$

which corresponds to a non-truncated trichromatic IR field with well defined phase and intensity relation between the three frequency components. As long as all the XUV pulses lie well within the region  $|t - t_{\text{IR}}| < \frac{\pi}{2\Omega}$ , the contributions to the signal that come from the other oscillations of the IR envelope can be safely neglected. This periodic configuration for the IR dressing field, therefore, is appropriate to simulate the case of a finite IR pulse. With this choice, the free photoelectron will be indefinitely driven by the IR field, with no consequences other than an irrelevant phase factor due to forward Compton scattering. The phase  $\Theta(t)$  in (2.6) for the Volkov state in the presence of a modulated IR is

$$\Theta(t) = \vec{\alpha}_0 \cdot \vec{k} \cos^2[\Omega(t - t_{\text{IR}})] \sin[\omega_{\text{IR}}(t - t_{\text{IR}}) + \varphi_{\text{IR}}] + o(\Omega/\omega_{\text{IR}}) + \text{const.} \quad (2.20)$$

The time-independent term *const* can be ignored, as we did in the case of equation (2.8). The higher-order correction  $o(\Omega/\omega_{\text{IR}})$  alters slightly the proportions of the monochromatic

components of the zeroth-order term. If needed, it can be taken into account exactly; yet, it can generally be safely neglected. If we do so, the three frequency components of  $\Theta(t)$  are

$$\Theta(t) \simeq \frac{\vec{\alpha}_0 \cdot \vec{k}}{4} \{ 2 \sin[\omega_{\text{IR}}(t - t_{\text{IR}}) + \varphi_{\text{IR}}] + \sin[(\omega_{\text{IR}} + 2\Omega)(t - t_{\text{IR}}) + \varphi_{\text{IR}}] \\ + \sin[(\omega_{\text{IR}} - 2\Omega)(t - t_{\text{IR}}) + \varphi_{\text{IR}}] \}, \quad (2.21)$$

so the Volkov phase factor for such a field is just the product of the Volkov factors for the three individual monochromatic field components [see (2.9)]

$$\Psi_{\vec{k}}(\vec{r}, t) \cong |\vec{k}\rangle \exp\left(-i\frac{k^2}{2}t\right) \sum_{\{n_i\}} J_{n_1}\left(\frac{x\xi}{2}\right) J_{n_2}\left(\frac{x\xi}{4}\right) J_{n_3}\left(\frac{x\xi}{4}\right) \\ \times \exp\{-in_{\text{tot}}[\omega_{\text{IR}}(t - t_{\text{IR}}) + \varphi_{\text{IR}}]\} \exp[-4i(n_3 - n_2)\Omega(t - t_{\text{IR}})], \quad (2.22)$$

where the sum runs over all the positive and negative integer values of the three  $n_i$  indexes,  $n_{\text{tot}} = n_1 + n_2 + n_3$ . The transition amplitude is finally

$$\mathcal{A}_{\vec{k} \leftarrow \text{g}} \cong -i\sqrt{2\pi} \alpha x k \phi_{\text{g}}(k) \sum_{\{n_i\}} J_{n_1}\left(\frac{x\xi}{2}\right) J_{n_2}\left(\frac{x\xi}{4}\right) J_{n_3}\left(\frac{x\xi}{4}\right) \quad (2.23)$$

$$\times \exp[in_{\text{tot}}(\varphi_{\text{IR}} + \omega_{\text{IR}}t_{\text{IR}}) - 2i(n_3 - n_2)\Omega t_{\text{IR}}] \\ \times \tilde{A}_{\text{XUV}} \left[ E_{\text{g}} - \frac{k^2}{2} - n_{\text{tot}}\omega_{\text{IR}} + 2(n_2 - n_3)\Omega \right]. \quad (2.24)$$

In the low intensity limit, we recover the two-photon transition amplitude from the lowest-order perturbative treatment in the plane-wave approximation. The integrated sideband signal is defined here as

$$I_{2n} = \int_{E_-}^{E_+} dE \int d\Omega \sqrt{2E} |\mathcal{A}_{\vec{k} \leftarrow \text{g}}|^2, \quad E_{\pm} = E_{\text{g}} + \frac{4n \pm 1}{2} \omega_{\text{IR}}. \quad (2.25)$$

This definition is justified as long as the photoelectron signal at the midpoints  $E_{\pm}$  between the sidebands and the adjacent harmonics is negligible, a condition fulfilled in all the cases considered in this work.

### 2.3. Frequency-comb limit

Key to the standard application of the RABITT technique is the lowest-order perturbative approximation where only one IR photon is assumed to be exchanged with the atom. At intensities of the order of  $1 \text{ TW cm}^{-2}$ , however, additional paths that imply the exchange of two or more IR photons become important. As a consequence, several transition matrix elements contribute to give rise to the variation of the photoelectron sideband intensity as a function of the time delay. In particular, on the side to the fundamental RABITT frequency  $2\omega_{\text{IR}}$ , several overtones  $2n\omega_{\text{IR}}$  appear, which have an involved relation with the phases of the harmonics in the train. For this reason, high intensities are generally considered detrimental to the resolution with which the RABITT technique can reconstruct the average profile of an attosecond pulse within the train [61]. This does not have to be necessarily the case, however, if a reliable correspondence between the sideband signal and the underlying harmonics beyond the lowest-order perturbative

regime can be established. To gain an insight into the dependence of the sideband signal on the intensity of the dressing laser, let us consider the limiting case of a frequency comb [62], i.e. of a very long sequence of very narrow XUV pulses. In this case, the spectrum of the field is locally given by a series of equally spaced narrow peaks with similar height. We can extrapolate the SPA to this limit, and obtain an analytical expression for the intensity of all the discrete frequency components of the sidebands as a function of the time delay. Let us assume that the comb Fourier spectrum has the following expression:

$$\tilde{A}_{\text{XUV}}(\omega) = A_0 \omega_{\text{IR}} \sum_{i=-\infty}^{+\infty} \tilde{g}[\omega - (2i+1)\omega_{\text{IR}}], \quad (2.26)$$

where  $\tilde{g}(\omega)$  is a sharp function centred in a small neighbourhood of  $\omega = 0$ , while the negative and positive indices account for photon absorption and stimulated emission, respectively. The expression in 2.26 is justified as long as the intensity of the high-harmonics spectrum does not change much across an energy interval of the same order as the classical excursion  $\Delta E$  of the kinetic energy of a free electron driven by the dressing field,  $\Delta E = 2\sqrt{8U_p E_e}$ , where  $U_p$  and  $E_e$  are the ponderomotive energy and the free-electron energy, respectively. If we focus on the sideband  $2m$ , the photoelectron signal is negligible unless the electron final kinetic energy lies in the close vicinity of  $E_g + 2m\omega_{\text{IR}}$ ,  $k^2/2 = E_g + 2m\omega_{\text{IR}} + \varepsilon$ . When inserted in (2.10), therefore, equation (2.26) gives rise to factors of the form

$$\tilde{g}[-(2m+n+2i+1)\omega_{\text{IR}} + \varepsilon], \quad (2.27)$$

which are non-negligible only if  $2m+n+2i+1=0$ . As a consequence, only net exchanges of an odd number  $n$  of IR photons can contribute. The amplitude in (2.10) is then,

$$\mathcal{A}_{\vec{k} \leftarrow g} \cong -i A_0 \omega_{\text{IR}} \sqrt{2\pi} \alpha k_{2m} \phi_g(k_{2m}) \tilde{g}(\varepsilon) \sum_n^{\text{odd}} x J_n(\xi x) e^{in\varphi_{\text{IR}}}, \quad (2.28)$$

where  $x$  is the cosine of the angle formed by  $\vec{\alpha}_0$  and  $\vec{k}_{2m}$ , and  $k_{2m} = (4m\omega_{\text{IR}} + 2E_g)^{1/2}$ . Both the pre-factor and the reduced field strength in (2.28) are smooth functions of the electron energy. Consecutive sidebands, therefore, have an almost identical energy profile that is largely insensitive to the intensity of the dressing laser. For the sake of conciseness, in the following, we render the dependence on the final energy implicit, drop the sideband index and refer to a generic sideband instead. The integral of the sideband signal is thus

$$I_{\text{SB}} = \beta \int_{-1}^1 x^2 dx \left| \sum_n^{\text{odd}} J_n(\xi x) e^{in\varphi_{\text{IR}}} \right|^2, \quad (2.29)$$

where  $\beta$  collects the fixed factors that depend on the details of the XUV spectrum but not on the IR intensity,

$$\beta = 2\pi |\alpha \omega_{\text{IR}} A_0 k_{2m} \phi_g(k_{2m})|^2 \int_0^\infty \sqrt{2\varepsilon} d\varepsilon |\tilde{g}(\varepsilon)|^2. \quad (2.30)$$

The integral in (2.29) determines the frequency composition of each and every sideband in the frequency-comb limit, due to the interference of the contributions arising from the net exchange of an arbitrary odd number of IR photons (see figure 3). We can reformulate the

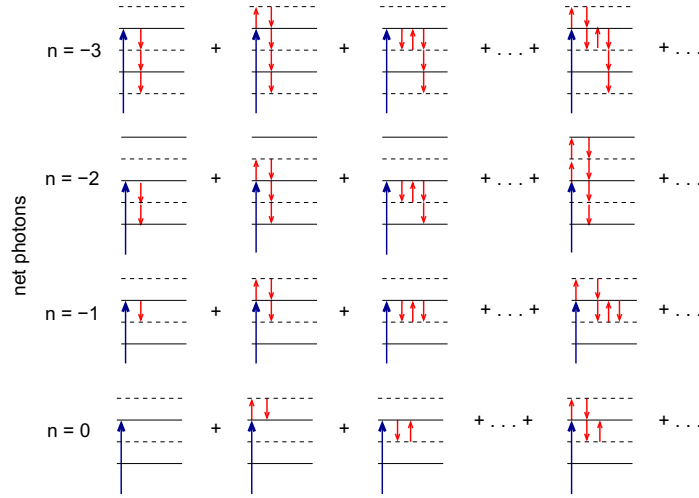


**Figure 3.** For intense dressing fields, several IR photons can be exchanged. For each amplitude that corresponds to a net number of IR photons absorbed or emitted, an infinite number of diagrams contribute. The SPA adds up to infinite order the contribution of all the time-ordered diagrams where the first absorbed photon is from the XUV field. The amplitude for a net exchange of  $n$  IR photons carries the phase  $n\varphi_{\text{IR}} = n\omega_{\text{IR}}t_d + \varphi_{\text{IR},0}$ . As a consequence, overtones at all even multiples  $2m\omega_{\text{IR}}$  of the dressing-laser fundamental frequency will appear in the time-delay dependence of the sideband intensity (only amplitudes with an odd net number of exchanged IR photons can contribute to the sidebands).

expression (2.29) by factorizing the dependence on the IR phase  $\varphi_{\text{IR}} = \omega_{\text{IR}}t_d$  (we assume a zero absolute IR phase  $\varphi_{\text{IR},0}$ ),

$$I_{\text{SB}} = \beta \sum_{j=0}^{\infty} C_j(\xi) \cos(2j \omega_{\text{IR}}t_d), \quad (2.31)$$

$$C_j(\xi) = \int_{-1}^1 \frac{2x^2 dx}{1 + \delta_{j0}} \sum_n^{\text{odd}} J_n(\xi x) J_{n+2j}(\xi x), \quad (2.32)$$

where the index  $j$  designates the sideband harmonic component, namely: average signal ( $j = 0$ ); fundamental RABITT frequency ( $j = 1$ ); first overtone ( $j = 2$ ); second overtone ( $j = 3$ ), etc. Equations (2.31) and (2.32) completely characterize the temporal profile of sideband intensities in the idealized case of a frequency comb pump sequence as a function of both the time delay and the IR intensity. The integral in (2.32) could be expressed in closed form in terms of special functions. The result, however, is rather lengthy and does not seem to provide further insight. As will be discussed in more detail at the end of section 3, a major feature of the  $C_j(\xi)$  coefficients is that, for  $j > 0$ , they oscillate around zero as a function of  $\xi$ , crossing the axis for different values of the reduced field strength. This means that the relative proportion of the frequency-component amplitudes of the sideband changes with the intensity. In fact, the fundamental RABITT component periodically vanishes altogether, a condition in which overtones dominate. Finally, if the sideband signal can be resolved along fixed directions in space (e.g.  $\cos \theta = 0$ ), the modulation of the corresponding overtone amplitudes, which are given by

the argument of the integrals in (2.32), is more pronounced than for the angularly integrated signal.

### 3. Results

Here, we will apply the analytical method described in section 2 and the *ab initio* numerical method described in appendix B to compute the photoelectron energy and angularly resolved distribution for photoionization of the helium atom from the  $1s^2$  ground state to the  $1s$  channel of the  $\text{He}^+$  parent ion in the energy region across the  $N = 2$  excitation threshold, within XUV-pump IR-probe schemes,

$$\text{He}(1s^2) + \gamma_{\text{XUV}} \pm n\gamma_{\text{IR}} \rightarrow \text{He}^+(1s) + e_k^-. \quad (3.1)$$

We will consider two cases: that of an XUV SAP and that of an APT.

#### 3.1. Single attosecond pulse case

Let us consider the case of an isolated sub-femtosecond XUV pulse overlapped with an intense IR pulse first. A characteristic feature of such experiments is the streaking effect, i.e. an overall shift  $\Delta\vec{p} = -\alpha\vec{A}_{\text{IR}}(t)$  of the momentum distribution of the photoelectron generated by an attosecond XUV pulse centred at time  $t$ . The streaking effect, which has a purely classical explanation, has been one of the first means to achieve control over the photoelectron ejection process [4]. Recently, the streaking effect has also been instrumental to detect the small time delay associated with photoemission [11, 44–51]. In this work, however, we will not consider this latter aspect, since it would enter the comparison between *ab initio* simulations and model predictions as only a minor correction to the more macroscopic features we are about to discuss. For XUV pulses with duration larger than the period of the IR dressing field, a transition from the streaking picture to the sideband picture, characteristic of monochromatic XUV fields [21], is observed. Kazansky *et al* [28] recently examined in detail this transition within the strong-field approximation. Here, we employ an XUV pulse with  $\text{fwhm}_{\text{XUV}} = 709$  as, comparable with a quarter of the IR period,

$$\vec{A}_{\text{XUV}}(t) = A_{\text{XUV},0} \hat{\epsilon} \frac{\exp\left[-\frac{(t-t_{\text{XUV}})^2}{2\sigma_{\text{XUV}}^2}\right]}{\sqrt{2\pi}\sigma_{\text{XUV}}} \cos(\omega_{\text{XUV}}t), \quad \sigma_{\text{XUV}} = (8 \ln 2)^{-1/2} \text{fwhm}_{\text{XUV}}, \quad (3.2)$$

a choice situated at the boundary between the streaking and the side-band limits. The other pulse parameters used in the simulation are:  $\omega_{\text{XUV}} = 61.8$  eV,  $I_{\text{XUV}} = 0.1$  TW cm $^{-2}$ ,  $\omega_{\text{IR}} = 1.55$  eV,  $I_{\text{IR}} = 1$  TW cm $^{-2}$  and  $\text{fwhm}_{\text{IR}} = 4.46$  fs. Both pulses are linearly polarized along the  $\hat{z}$  direction. We conducted simulations for three values of the carrier-envelope phase (CEP) of the IR pulse:  $0^\circ$ ,  $45^\circ$  and  $90^\circ$ . In the three cases, the centres of the XUV and the IR pulse coincide (zero time-delay). Since the duration of the XUV pulse is much shorter than the fwhm of the IR pulse, by changing the CEP we reproduce the case of a longer IR pulse where the time delay is changed instead. This approach is useful when conducting computationally intensive simulations because it permits one to use short IR pulses thus keeping the overall propagation time to a minimum. The predictions of the SPA model were computed by using the same set of parameters as in the simulation, with the exception of the fwhm of the IR field, which in this case is assumed to be monochromatic. In figure 4, we compare the photoelectron spectra resulting from the

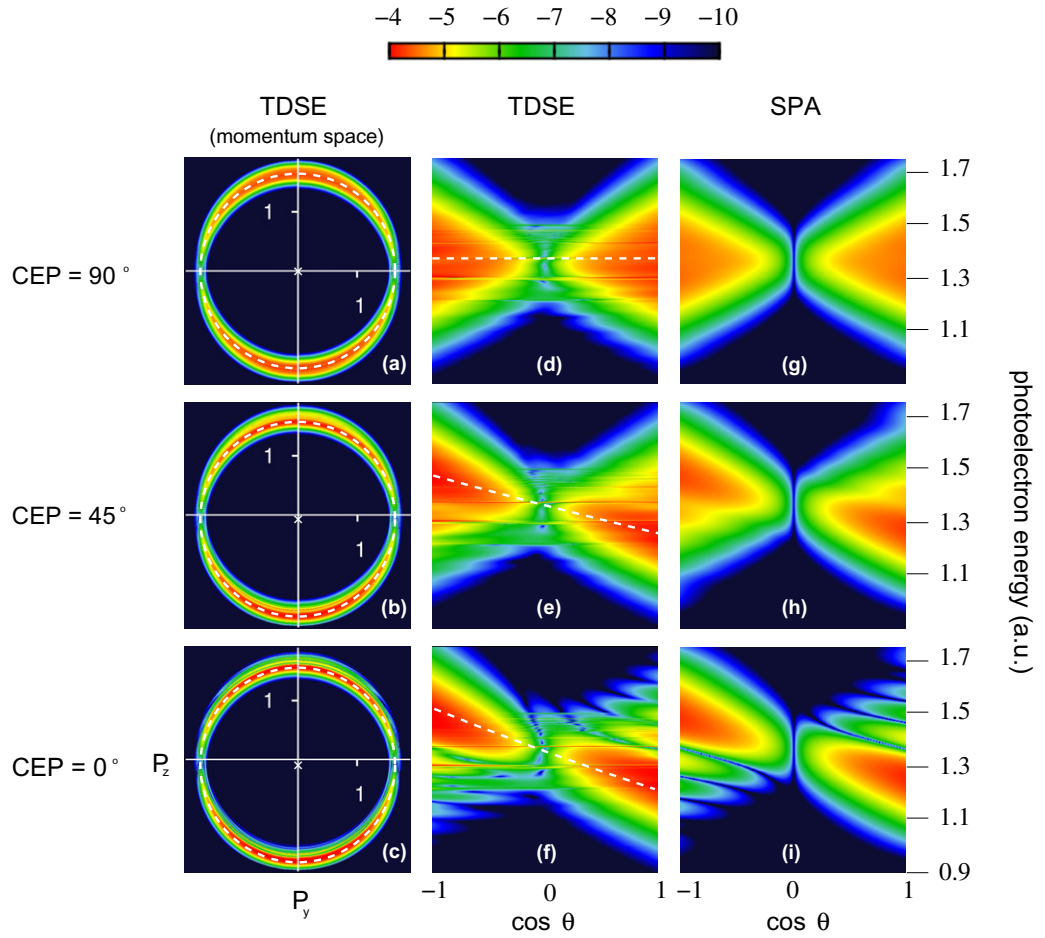


**Figure 4.** Comparison of photoelectron spectra in the 1s channel obtained by direct integration of the TDSE (a)–(f) with the prediction of the SPA (g)–(i) for the case where a helium atom is ionized by a SAP with central energy 61 eV in the presence of an IR field ( $\lambda_{\text{IR}} = 800 \text{ nm}$ ,  $I_{\text{IR}} = 1 \text{ TW cm}^{-2}$ ) at zero time delay. The three panel rows correspond to three different values of the cosine-modulated IR CEP: 90°, 45° and 0°. First column: section of the photoelectron momentum distribution in the  $yz$  plane. Second column: same distribution as in the first column but in the representation photoelectron energy versus cosine of the photoelectron ejection angle with respect to the laser polarization. Third column: prediction of the monochromatic SPA. The colour code is on a  $\log_{10}$  scale. The reported signal is a probability density per unit of cubic linear momentum (first column) or per unit of energy (second and third column), in atomic units.

*ab initio* calculations (figures 4(a)–(f)) with those from the SPA model (figures 4(g)–(i)). The latter have been scaled by a common factor to closely match the absolute value obtained from the simulation. In all the cases, the colour-code corresponds to a logarithmic scale. The three panels on the left column (figures 4(a)–(c)) show the photoelectron distribution in the ( $p_x$ ,  $p_z$ ) plane as it would appear after reconstruction [63] from the experimental data recorded with a



velocity-map imaging detector [64]. A dashed circle on top of the data, centred on the white cross along the vertical axis, indicates the expected position of the signal predicted by the streaking formula. To appreciate the distribution details in a better manner, the panels in the middle column (figures 4(d)–(f)) illustrate the same quantity as in the left column in a energy versus  $\cos \theta$  representation, where  $\theta$  is the photoelectron ejection angle with respect to the laser polarization. We can recognize four characteristic features. (I) Two dominant lobes, centred at  $\omega_{\text{XUV}} - \text{IP}$  in the case of  $\text{CEP} = 0^\circ$ , which (II) follow a clear streaking trajectory as the CEP of the dressing field is changed. In this representation and for the current IR intensity, the streaking effect appears as a tilt in the distribution. The prediction of the streaking formula is indicated with a dashed line. (III) For the case where the streaking is largest (figure 4(f)), sidebands appear below the left and above the right lobe. Finally, (IV) narrow horizontal resonant features, due to the presence of doubly excited states, are visible. The three panels in the right column (figures 4(g)–(i)) show the prediction of the SPA. The first three-dominant features of the *ab initio* angularly resolved spectra, (I–III), are accurately reproduced. In particular, the sidebands in figure 4(f) are an interference effect of quantum streaking (figure 4(i) is analogous to figure 4(a) in [28]) instead of a consequence of the presence of intermediate doubly excited states. Such an interference effect is due to the fact that, if the duration of the SAP used in the pump–probe ionization is comparable with the half period of the IR, the streaking is not uniform across the pulse. When the centre of the XUV pulse coincides with the zero of the vector potential (figures 4(a), (d) and (g)), the IR accelerates the photoelectrons ejected in any given direction upwards during the first half of the XUV pulse and downwards during the second half. As a consequence, the spectrum of the photoelectron is widened. Furthermore, the wave-packet in the upward direction acquires a negative chirp (not visible in the energy-resolved signal) while the one heading downward acquires a positive chirp. In the case the centre of the XUV pulse coincides with the maximum of the vector potential (figures 4(c), (f) and (i)), the energy bandwidth in either the lower or the upper lobe is smaller than in the previous case. The ionization amplitude generated at times  $t_1 = t_{\text{XUV}} - \Delta t/2$  and  $t_2 = t_{\text{XUV}} + \Delta t/2$  which are symmetric with respect to the XUV pulse centre are equally streaked by the IR, leading to the interference fringes above the upper and below the lower lobe. Two additional general aspects of the comparison between the *ab initio* and model spectra in figure 4 are worth mentioning. Firstly, while in the SPA model the probability of ejecting one electron in the plane orthogonal to the laser polarization is always zero (see, e.g. equation (2.10)), this is generally not the case for the results from the TDSE, where a small but noticeable departure from zero is visible also for  $\cos \theta = 0$ . The reason for this difference can be attributed both to the single-particle effects not contemplated by the model (i.e. combined action of the IR and of the Coulomb field) and to multi-particle effects like the resonant excitation of even-parity autoionizing states (e.g.  $^1\text{S}^e$  resonances below the  $N = 2$  threshold decay to the  $1s$  channel by isotropic photoelectron emission), or the virtual excitation of the  $N = 2$  channels (polarization of the initial state and of the parent ion). Secondly, the SPA model provides a remarkably good representation for the  $1s$  photoelectron spectrum even above the  $N = 2$  threshold at  $E_e = 1.5$  au, where the  $2s$  and  $2p$  channels are open. This circumstance illustrates that, if the inter-channel coupling is weak, the SPA is still applicable to the one dominating channel. This example illustrates how the SPA can be used to reproduce with remarkable accuracy most of the background features of photoelectron angular distributions in realistic systems, even in the presence of transiently bound states. Since the optical transition to these states from the ground state is forbidden at the level of the independent particle model, their influence in the spectrum is comparatively

minor. The role of doubly excited states and threshold opening on the photoelectron spectrum is beyond the scope of this work and will be the subject of a future publication.

### 3.2. Attosecond pulse train case: effect of finite probe duration

Let us now consider the case of a train of attosecond pulses comprising of a sequence of Gaussian XUV pulses, with central energy  $\omega_{\text{XUV}} = 60.29 \text{ eV}$  and  $\text{fwhm} = 192 \text{ as}$ , separated by half the period of the IR probe pulse and with alternating sign; the train envelope has a duration of 6 fs and a maximum intensity  $I_{\text{XUV}} = 0.1 \text{ TW cm}^{-2}$ . As in the SAP, we conduct the *ab initio* simulation with a short ( $\text{fwhm}_{\text{IR}} = 5.36 \text{ fs}$ ) moderately intense ( $I_{\text{IR}} = 1 \text{ TW cm}^{-2}$ ) IR pulse. On the one hand, as anticipated in previous sections, the use of a short IR pulse significantly reduces the computational burden while at the same time reproducing most of the features observed in realistic experiments, in which the length of the IR pulse associated with XUV trains is often larger. On the other hand, since the duration of the XUV train and the IR pulse are now comparable, some effects due to the fact that the IR intensity is not uniform across the train are to be expected. For a meaningful comparison with the experiment, therefore, it is important to be able to identify and factor out such effects. In figure 5, we compare the photoelectron angular distribution for a fixed time delay  $t_d = -T_{\text{IR}}/4 = -0.666 \text{ fs}$  computed with: (a) *ab initio* simulation, (b) SPA model with a monochromatic IR field and (c) SPA model with a pulsed IR field. All the three methods predict a minimum in the harmonic signal at  $\sim 60^\circ$  from the polarization axis. This is an extreme example of the angular broadening observed experimentally and reproduced with single-active-electron simulations by Guyetand *et al* [65]. In [66], the phenomenon was justified on the basis of a truncated perturbative expansion of the SPA. Indeed, third-order corrections to the harmonic amplitude that come from the absorption or emission of two IR photons have an angular distribution proportional to  $\cos^3 \theta$ . The interference term with the first-order amplitude, which is proportional to  $\cos \theta$ , therefore, gives rise to a  $\cos^4 \theta$  term which alters the harmonic signal predominantly along the polarization axis. The agreement of the monochromatic model (figure 5(b)) with the simulation (figure 5(a)), however, is not as impressive as for the SAP. In the simulation, the odd-harmonics signals next to the polarization axis are clearly split, a feature that the monochromatic model does not reproduce. That this feature is due to the finite duration of the probe pulse and not to the correlated electron dynamics in the atom is clearly demonstrated by the impressive agreement with the third panel, obtained with the pulsed SPA model. Indeed, apart from the missing narrow resonant lines associated with He doubly excited states, the pulsed model is able to reproduce all of the most prominent background features of the simulated spectrum. In conclusion, the use of short dressing pulses is reflected in both the angular and energy distribution of the photoelectrons. When assessing the influence of Coulomb or many-body corrections on the photoelectron spectrum, therefore, comparison with the monochromatic soft-photon model can be misleading; the effects of a finite pulse duration may need to be taken into account.

Figure 6 compares the angularly integrated photoelectron spectra computed with *ab initio* simulations and with the pulsed SPA model for five different time delays between the two pulses:  $-1.33$ ,  $-0.67$ ,  $0$ ,  $0.67$  and  $1.33 \text{ fs}$  (figures 6(a) through (e), respectively). Again, apart from the resonant features, the agreement between model and simulation is very good across the whole IR period and energy range. In conclusion, the pulsed version of the SPA model is able to reproduce the consequences of a finite duration of the IR dressing pulse on the fully differential photoelectron distribution. Possible application of such extended model include interpretation

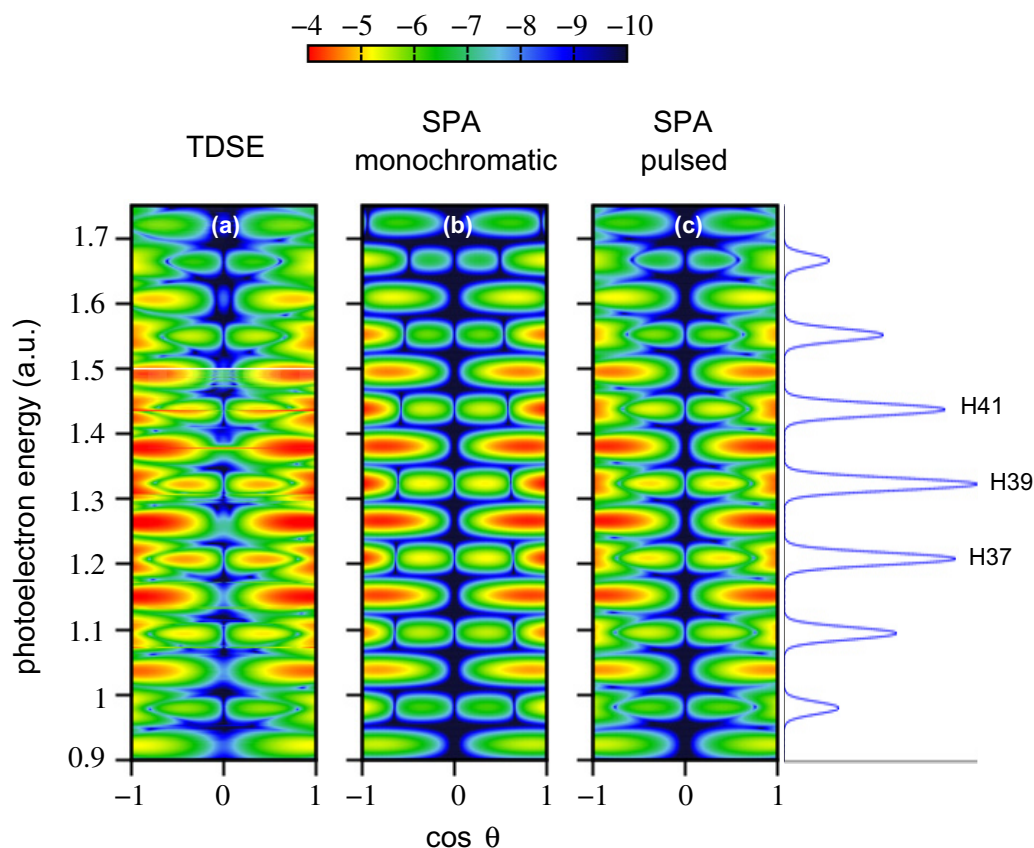


**Figure 5.** Calculated photoelectron spectra for the case where a helium atom is ionized by an APT with energy 61 eV in the presence of an IR field ( $\lambda_{\text{IR}} = 800$  nm,  $I_{\text{IR}} = 1$  TW cm $^{-2}$ ). Panel (a) represents the full calculation of the TDSE, using a cosine-square envelope for the IR probe pulse, while panels (b) and (c) were calculated using the SPA for: (b) a monochromatic IR pulse and (c) a cosine-square modulated IR pulse.

of photoelectron angular distributions in real experiments, refinements of the RABITT protocol and assistance in the interpretation of *ab initio* simulation in the presence of features beyond the reach of a single-active-electron model, like autoionizing states and above-threshold multi-channel interactions.

### 3.3. Attosecond pulse train case: effect of high probe intensity

The variation of sideband intensity as a function of the time delay is a major observable in pump-probe experiments based on the use of APT. In the following, we shall examine how such variation is affected by the intensity of the dressing field. To focus on this aspect without the interference of either finite-pulse or correlation effects, we will consider the monochromatic version of the SPA model only. As long as the IR pulse is longer than 3–4 times the APT duration, this approximation is justified. In figure 7, we report the photoelectron spectrum computed with the monochromatic and pulsed version of the SPA model in the case of an APT with the same parameters as in figure 6(b) but where the IR pulse has a much larger duration,

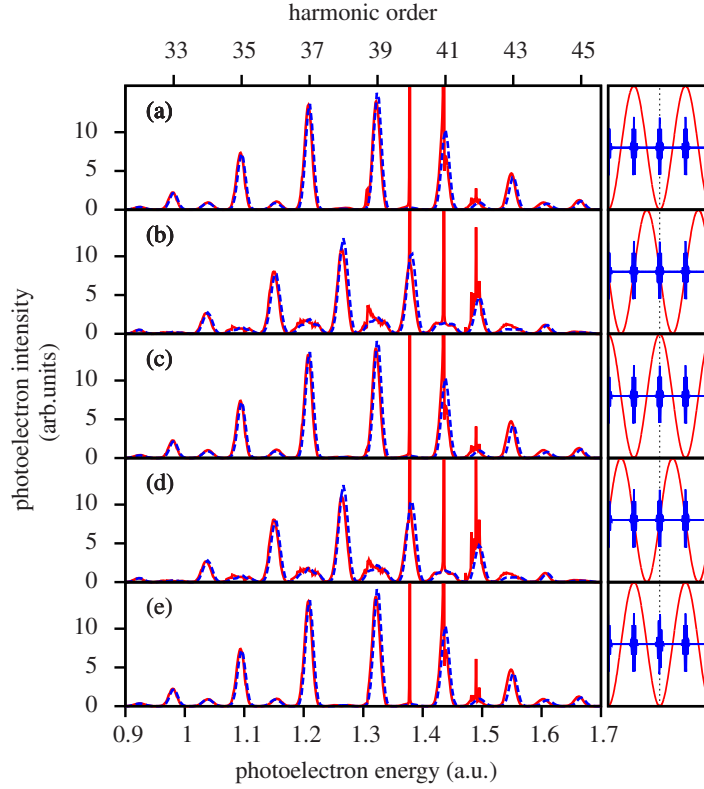


**Figure 6.** Total photoelectron distribution of a helium atom ionized by an attosecond XUV pulse train of central frequency 61 eV in the presence of an IR dressing pulse ( $\lambda_{\text{IR}} = 800 \text{ nm}$ ,  $I_{\text{IR}} = 1 \text{ TW cm}^{-2}$ ) for five different time stages: (a) XUV at the minimum of the vector potential; (b) XUV at inflection point; (c) XUV at maximum of vector potential; (d) XUV at inflection point (half an IR period later than case (b)); and (e) XUV at minimum of vector potential (one IR period later than in case (a)). Red solid line: numerical solution of the TDSE. Blue dashed line: pulsed SPA model.

$\text{fwhm}_{\text{IR}} = 21.78 \text{ fs}$ . In these conditions, the consequences of a finite duration of the IR pulse are indeed sufficiently small to leave the most prominent features of the photoelectron spectrum dependence on laser intensity unaltered.

In the weak-field limit, the sideband signal is known to oscillate at the fundamental RABITT angular frequency  $2\omega_{\text{IR}}$ . As discussed in section 2, however, as the intensity of the dressing field is raised, overtone components with angular frequency  $2n\omega_{\text{IR}}$  start to appear. Figures 8(a)–(e) (left panels) show the integrated intensity of a central sideband as a function of the time delay across half a period of the IR for several values of the IR reduced field strengths  $\xi$ . For each intensity, three curves are plotted: one obtained with the analytical formulae in the frequency-comb limit, and two others computed with the monochromatic SPA model with the parameters chosen either to approach the frequency-comb limit ( $\text{fwhm}_{\text{XUV}} = 50 \text{ as}$  and  $\text{fwhm}_{\text{APT}} = 24 \text{ fs}$ ) or to reproduce ordinary experimental APT parameters ( $\text{fwhm}_{\text{XUV}} = 263 \text{ as}$  and  $\text{fwhm}_{\text{APT}} = 11 \text{ fs}$ ). Even for moderate field strengths, the time-delay dependence of the sideband signal deviates significantly from the characteristic sinusoidal modulation of the weak-field limit (1.1).

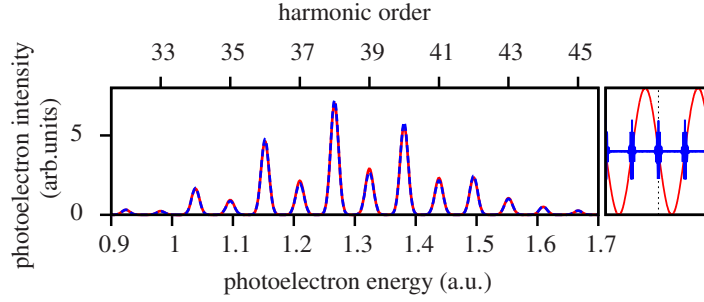


**Figure 7.** Photoelectron energy spectrum for the ionization of the helium atom from the ground state by means of a RABITT pump–probe scheme, computed with two different models: monochromatic SPA (red solid line) and pulsed SPA (blue dashed line). The pulse parameters are the same as in figure 6 except for the modulation of the IR field in the pulsed model, which here reproduces an IR pulse with duration much larger than that of the APT,  $\text{fwhm}_{\text{IR}} = 21.78$  and  $\text{fwhm}_{\text{APT}} = 6$  fs. In these conditions, the boundary effects associated with the finite duration of the dressing field (pulsed case) are negligible: the spectrum is well reproduced within the infinite-pulse approximation (monochromatic case).

For values of the reduced field strength of the order of 3 ( $I_{\text{IR}} \sim 5 \text{ TW cm}^{-2}$  at  $E_e = 2 \text{ au}$ ), multiple maxima start to appear. In the case of a realistic APT, the sharp modulations predicted in the frequency-comb limit are somewhat washed out as a consequence of the finite energy span and duration of the APT. Yet, even with these realistic pulses, the qualitative change of the profile is still clearly visible. It should be noted that in the present treatment we are neglecting the electrons which tunnel out of the atom as a result of the dressing field alone. The energy of these electrons has an ultimate cutoff around ten times the ponderomotive energy [67]. A conservative estimate of the largest intensity that can be achieved without the spectrum of the tunnelling electron overlapping that of the photoelectrons is  $I(\text{au}) < \frac{\omega_{\text{IR}}^3}{4\pi\alpha} \frac{1}{\sqrt{20}} \xi$ . It should also be noted, however, that the photoelectron signal scales linearly with the intensity of the XUV pulse. Acting on the latter, therefore, it is in principle still possible to disentangle the two processes even for larger intensities of the dressing laser.

The time dependence of the sidebands can be parameterized in terms of a discrete Fourier series which, for parity reasons, comprises only even multiples of the IR fundamental frequency (see equation (2.31))

$$I_{\text{SB}}(t; \xi) \propto \sum_{j=0} \cos(2j\omega_{\text{IR}}t) C_j(\xi). \quad (3.3)$$

In section 2 we derived an analytical expression for the amplitudes  $C_j(\xi)$  of the harmonic components in the frequency comb limit. Figures 8(f)–(i) (right panels) show the coefficients of the average sideband signal  $C_0$ , of the fundamental RABITT modulation  $C_1$ , and of the first two overtones  $C_2$  and  $C_3$ , as a function of the reduced field strength for the same three models used in the left panels. The most striking feature of these plots is that all the  $C_j(\xi)$  amplitudes are predicted to oscillate periodically as the intensity of the laser increases. In particular, the fundamental modulation  $C_1$  below  $\xi = 10$  ( $I_{\text{IR}} \simeq 10^{14} \text{ W cm}^{-2}$  for  $E_e = 1 \text{ au}$ ) changes sign five



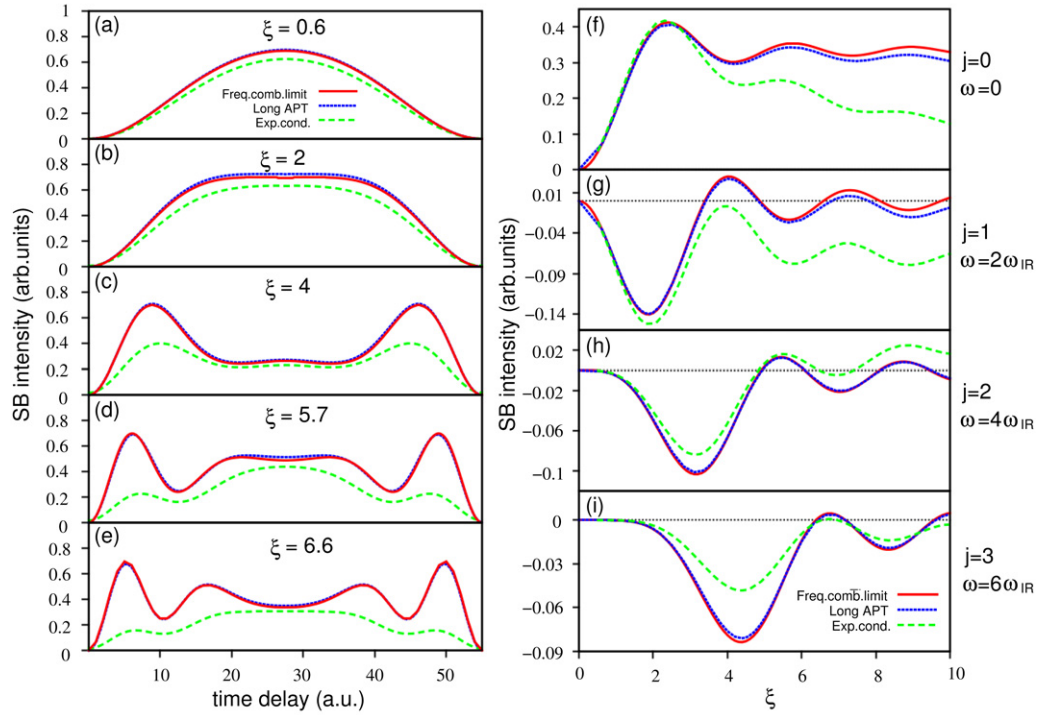


**Figure 8.** Left panels (a)–(e): energy integrated photoelectron signal of a central sideband as a function of the time delay between an XUV APT and a monochromatic IR probe for five different values of the reduced field strength  $\xi$ ; from top to bottom:  $\xi = 0.6, 2, 4, 5.7$  and  $6.6$ . Frequency comb limit: solid red line; SPA for an XUV APT is close to the frequency comb limit (train duration = 24 fs and pulse duration = 50 as): dotted blue line; SPA for an XUV APT with common experimental parameters (train duration = 11 fs and pulse duration = 263 as). Right panels (f)–(i): coefficients  $C_j(\xi)$ ,  $j = 0, 1, 2$  and  $3$  (top to bottom) of the harmonic components of the time-dependent integrated sideband signal (see text), as functions of the reduced field strength  $\xi$ , for the same three models as in the left panels.

times in the frequency comb limit, and even for the shortest APT it vanishes almost entirely for  $\xi \simeq 4$  ( $I_{\text{IR}} \simeq 8 \text{ TW cm}^{-2}$  for  $E_e = 2 \text{ au}$ ). Close to these intensities, overtones dominate. In [61], L’Huillier and co-workers reported measurements of the phase of the  $4\omega_{\text{IR}}$  and of the  $6\omega_{\text{IR}}$  overtones. Therefore, even if the authors did not report or comment on the dependence of the amplitude of the overtone components on the laser intensity, the determination of the oscillations shown in figure 8(b) should be well within the reach of current laser technology. In [61], the authors concluded that the appearance of overtones was to be associated with a loss of accuracy and a bias towards artificially compressed attosecond pulses in the RABITT reconstruction protocol. In fact, within the SPA it is possible to keep track of all the sideband frequency components even for large intensities, as soon as the experimental contrast and time-delay resolution is sufficiently high. The frequency-comb limit of the SPA can thus conceivably be the basis for an extension of the RABITT protocol to non-perturbative regimes.



#### 4. Conclusions

In this work we have shown that the SPA formulated for finite pump pulses and for a pulsed dressing field can accurately reproduce all the background features of the fully differential photoelectron angular distribution for the single photoionization of the helium atom in the energy region close to 1.5 au above the first ionization threshold, with the field parameters reproducing realistic attosecond-XUV-train pump/IR-probe experimental conditions. We have found that the angular distribution within the harmonics along the polarization is split as a consequence of the finite duration of the dressing field. We have derived an analytical expression in the frequency-comb limit for the integrated sideband intensity overtones' amplitudes which indicates that each amplitude oscillates as a function of the dressing-laser strength. In particular, the fundamental  $2\omega_{\text{IR}}$  component monitored in the RABITT technique is found to change sign periodically, and hence to vanish for certain intensities of the field. All the aforementioned results should be easily observable experimentally. We trust that the present results could be useful to extend the range of validity of the RABITT protocol to larger intensity ranges for field-metrology purposes as well as to assist in the interpretation of the background features in pump-probe protocols which make use of APT in combination with strong dressing fields for quantum-control purposes, possibly in the presence of metastable intermediate states.

#### Acknowledgments

We thank Professor Alfred Maquet, Dr Richard Taïeb and Dr Marcus Dahlström for fruitful discussions. We thank Mare Nostrum BSC and CCC-UAM (Centro de Computación Científica, Universidad Autónoma de Madrid) for allocation of computer time. The research leading to these results has received funding from the European Research Council under the European Union's Seventh Framework Programme (FP7/2007-2013)/ERC grant agreement number 290853, the European COST Actions CM0702 and CM1204, the ERA-Chemistry project number PIM2010EEC-00751, the Marie Curie ITN CORINF and the MICINN projects numbers FIS2010-15127 and CSD 2007-00010 (Spain).

#### Appendix A. Perturbative RABITT amplitude

Following standard lowest-order time-dependent perturbation theory [56], the total two-photon transition amplitude  $\mathcal{A}_{2n}^{(2)}$  giving rise to the sideband  $2n$  in the RABITT pump-probe scheme is the sum of the amplitudes for the four diagrams depicted in figure 1, and can be readily written as

$$\begin{aligned}\mathcal{A}_{2n}^{(2)} &= \mathcal{A}_1 + \mathcal{A}_2 + \mathcal{A}_3 + \mathcal{A}_4 \\ &= \frac{\pi}{2i} (A_{2n-1} A_{\text{IR}} \mathcal{M}_{2n-1} + A_{2n+1} A_{\text{IR}}^* \mathcal{M}_{2n+1}) \delta_T(E - \omega_g - 2n\omega).\end{aligned}\quad (\text{A.1})$$

In (A.1) we introduced the two-photon transition matrix elements  $\mathcal{M}_{2n\pm 1}$  for the absorption of the  $2n \pm 1$  harmonics,

$$\mathcal{M}_{2n\pm 1} = \langle E | P [G_0^+(\omega_g \mp \omega) + G_0^+(\omega_g + \omega_{2n\pm 1})] P | i \rangle, \quad (\text{A.2})$$

where  $|i\rangle$  is the initial state of the atom,  $|E\rangle$  is a final state in the continuum with appropriate symmetry,  $G_0^+(\omega) = (\omega - H_0 + i0^+)^{-1}$  is the retarded resolvent of the field-free

atomic Hamiltonian,  $P$  is the total electronic canonical momentum along the field polarization axis (we assume collinear polarization for all the external fields). The two-photon transition matrix elements are complex quantities; their argument is known as *atomic phase*,  $\varphi_n^{\text{At}} = \arg \mathcal{M}_n$ . The factors  $A_{\text{IR}}$  and  $A_{2n\pm 1}$  are the peak amplitude of the vector potential of the IR and of the two harmonics. Finally, the special function  $\delta_T(\omega)$  is defined as

$$\delta_T(\omega) = \frac{\sin \omega T/2}{\pi \omega}, \quad \lim_{T \rightarrow \infty} \frac{2\pi}{T} \delta_T^2(\omega) = \delta(\omega). \quad (\text{A.3})$$

The integral transition rate to a given sideband  $2n$ , therefore, is given by

$$\mathcal{W}_{2n}^{(2)} = \frac{1}{T} \int dE \left| \mathcal{A}_{2n}^{(2)}(E) \right|^2 = \frac{\pi}{8} \left| A_{2n-1} A_{\text{IR}} \mathcal{M}_{2n-1} + A_{2n+1} A_{\text{IR}}^* \mathcal{M}_{2n+1} \right|^2. \quad (\text{A.4})$$

If we use the APT as a reference to define the temporal scale, and thus keep it fixed with respect to the time delay, then the phases of the harmonics field amplitudes do not change with the time delay, while the phase of the IR, which we can here assume to be very long, is linear with the time delay:

$$A_{2n\pm 1} = |A_{2n\pm 1}| e^{-i\phi_{2n\pm 1}}, \quad A_{\text{IR}} = |A_{\text{IR}}| e^{-i(\varphi_{\text{IR},0} + \omega \tau)}. \quad (\text{A.5})$$

Inserting these latter parameterizations in the expression (A.4) for the transition rate to the sideband, and expressing the module of the vector potential amplitude in terms of the photon flux  $\Phi$

$$|A| = \frac{\sqrt{8\pi \Phi c}}{\omega}, \quad (\text{A.6})$$

we finally obtain (1.1)

$$\begin{aligned} \mathcal{W}_{2n\omega}^{(2)} = \frac{8\pi^3}{\omega_{\text{IR}}} \Phi_{\text{IR}} \Big\{ \Phi_{2n-1} |\mathcal{M}_{2n-1}|^2 + \Phi_{2n+1} |\mathcal{M}_{2n+1}|^2 \\ + 2\sqrt{\Phi_{2n-1} \Phi_{2n+1}} |\mathcal{M}_{2n-1} \mathcal{M}_{2n+1}| \cos \left[ \Delta\phi_{2n} + \Delta\varphi_{2n}^{\text{At}} - 2(\varphi_{\text{IR},0} + \omega_{\text{IR}} \tau) \right] \Big\}, \end{aligned} \quad (\text{A.7})$$

where  $\Delta\phi_{2n} \equiv \phi_{2n+1} - \phi_{2n-1}$  and  $\Delta\varphi_{2n}^{\text{At}} = \varphi_{2n+1}^{\text{At}} - \varphi_{2n-1}^{\text{At}}$ . If the properties of the ionization continuum do not change much across the energy span of a few  $\omega$ 's, as it is generally the case for rare gases in the energy region far from the ionization threshold, on the one side, and far from the autoionizing states, on the other side, then the two integrals  $\mathcal{M}_{2n+1}$  and  $\mathcal{M}_{2n-1}$  are similar both in absolute value and in phase. In particular, the atomic phase can be accurately linearized across the whole energy interval:  $\varphi_{2n-1}^{\text{At}} - \varphi_{2n+1}^{\text{At}} \simeq 2\omega_{\text{IR}} \partial_E \varphi_E^{\text{At}}$ . As a result, the phase of the sideband can be written as

$$\Phi_{2n} = \phi_{2n+1} - \phi_{2n-1} - \varphi_{\text{IR},0} - 2\omega_{\text{IR}} \partial \varphi_E^{\text{At}} / \partial E. \quad (\text{A.8})$$

Both the absolute value of the IR phase and the (typically small) value of the atomic phase change are unknown constants. If these constants are known, then the individual differences  $\phi_{2n+1} - \phi_{2n-1}$  can be determined and, from these, by means of an inverse discrete Fourier transform, the envelope of the whole train can be determined in absolute terms. Even if the absolute value of the IR phase or the energy derivative of the atomic phase are unknown, it is still possible to determine the average shape of the envelope of an attosecond pulse in the train, and in particular its duration, from all the values of  $\Phi_{2n} - \Phi_{2n-2}$ .

## Appendix B. *Ab initio* calculation of photoelectron spectra

To reproduce with high accuracy, photoelectron distributions differential in both energy and angle, we represent the atomic wave function on a  $B$ -spline close-coupling basis that is essentially complete in the dynamic regimes driven by the external fields under consideration. Starting from the ground, the state of the atom is propagated under the action of a given sequence of external XUV and IR ultrashort pulses by integrating the TDSE numerically. At the end of the simulation, as soon as the external pulses are over, we extract the distribution of the photo-fragments by projecting the wave-packet on a complete set of scattering states of the field-free atomic Hamiltonian. In the following, we describe briefly how these steps are carried out. More details on the time-dependent close-coupling procedure we use are available in the literature [31, 68, 69].

The close-coupling basis comprises of several partial-wave channels (PWC), defined as the antisymmetrized coupled product of a bound state of the  $\text{He}^+$  parent ion and of an electron state with well defined orbital angular momentum

$$\phi_{\alpha E} = \hat{A} \Theta_{S\Sigma} \mathcal{Y}_{L_\alpha \ell_\alpha}^{LM}(\Omega_1, \Omega_2) R_{N_\alpha L_\alpha}(r_1) \frac{f_{\alpha E}(r_2)}{r_2}, \quad (\text{B.1})$$

where  $\alpha$  is an index that uniquely identifies the PWC,  $\hat{A}$  is the antisymmetrizer,  $\Theta_{S\Sigma}$  is a two-electron spin function with total spin  $S$  and spin projection  $\Sigma$ ,  $\mathcal{Y}_{L_\alpha \ell_\alpha}^{LM}$  is a bipolar spherical harmonics [70] with total angular momentum  $L$  and projection  $M$ ,  $R_{N_\alpha L_\alpha}$  is the radial part of the frozen  $\text{He}^+$  parent ion state with principal quantum number  $N_\alpha$  and angular momentum  $L_\alpha$ . Finally,  $f_{\alpha E}$  is the radial function of the second electron, which is associated with the orbital angular momentum  $\ell_\alpha$ , but is otherwise unconstrained. All the radial functions are expressed in terms of  $B$ -splines, a numerical tool that is capable of representing arbitrary atomic orbitals on finite intervals with high accuracy [71–73]. In the present calculation, the grid of nodes defining the  $B$ -splines has been optimized to faithfully reproduce both the short-range behaviour of correlated localized states as well as the long-range rapidly-oscillating behaviour of the scattering functions up to a maximum box radius  $R_{\text{box}} = 1200$  au. Such a large box size is necessary in order to contain the fast outgoing electrons ( $\sim 40$  eV) generated by the pump, for the whole duration of the IR pulse. The asymptotic spacing between consecutive knots is 0.5 au.

In any actual implementation, the close-coupling expansion must be truncated. Furthermore, the set of bound states of the parent ion is not complete in the first place. As a consequence, PWCs alone are not sufficient to fully represent the correlated two-electron single-ionization space of helium. The missing contribution of the single- and double-ionization closed channels that are not included in the close coupling expansion, and which account for the short-range correlation between the two electrons, however, decays exponentially for increasing values of the radius of either electrons. To compensate for this missing component and attain both convergence and good accuracy, therefore, it is sufficient to include in the basis a *full-CI* pseudo-state localized channel (LC) comprising of a large number of normalized two-electron functions built from localized orbitals. Since we are focusing on an energy region well below the  $N = 3$  level of the  $\text{He}^+$  parent ion, we limit the close coupling expansion to the PWCs with  $N \leq 2$ :  $1sE_L$ ,  $2sE_L$ ,  $2pE_{L+1}$  and  $2pE_{L-1}$  (the latter being present only for non-zero total angular momentum  $L$ ). At the moderate IR intensities considered here ( $I_{\text{IR}} \leq 10^{13} \text{ W cm}^{-2}$ ), a total angular momentum of up to  $L = 9$  is sufficient to ensure convergence. Short-range correlation in the energy region of interest was found to be adequately taken into account by constructing the

LC from orbitals with maximum radius  $R_{\text{loc}} \simeq 40$  au and with a maximum angular momentum  $\ell_{\text{max}} = 5$  for  $L \leq 2$  and  $\ell_{\text{max}} = 4$  for  $3 \leq L \leq 8$ . Short-range correlation states for  $L = 9$  were neglected altogether. The number of linearly independent PWC and LC basis functions with well defined  $S$ ,  $\Sigma$ ,  $L$ ,  $M$  and parity obtained with this choice of parameters is comprised of a minimum of 9064 for the  $^1S^e$  symmetry and a maximum of 13 498 for the  $^1D^e$  symmetry.

The field-free electrostatic Hamiltonian of the atom,

$$H_0 = \frac{p_1^2}{2} + \frac{p_2^2}{2} - \frac{2}{r_1} - \frac{2}{r_2} + \frac{1}{r_{12}}, \quad (\text{B.2})$$

is projected on the close-coupling basis; each  $^{2S+1}L^\pi$  block is fully diagonalized, and the matrix elements of the dipole operator  $\vec{P} = \vec{p}_1 + \vec{p}_2$  between blocks are computed. The resulting ground-state energy,  $E_g = -2.903\,602\,76$ , is very close to the theoretical electrostatic value in the limit of a complete radial basis for the same maximum orbital angular momentum  $\ell_{\text{max}} = 5$ ,  $E_g^{\ell \leq 5} = -2.903\,605\,71$  [74] (the exact electrostatic limit is  $E_g^\infty = -2.903\,724\,38$  [75]). The eigenstates of  $H_0$  are thus obtained from the basis for the time propagation.

To compute the effect of the external fields on the ground state  $\Psi_g$  of the atom, we need to solve the TDSE,

$$i\partial_t \Psi(t) = [H_0 + \alpha \vec{A}(t) \cdot \vec{P} + V_{\text{abs}}] \Psi(t), \quad \lim_{t \rightarrow -\infty} e^{iE_g t} \Psi(t) = \Psi_g, \quad (\text{B.3})$$

where  $\vec{A}(t)$  is the total vector potential. To prevent unphysical reflections from the box boundary during the time propagation, we included in the total time-dependent Hamiltonian an absorption potential  $V_{\text{abs}}$  defined as

$$V_{\text{abs}}(\vec{r}_1, \vec{r}_2) = v_{\text{abs}}(r_1) + v_{\text{abs}}(r_2), \quad (\text{B.4})$$

$$v_{\text{abs}}(r) = -i c_{\text{abs}} \theta(r - R_{\text{abs}}) (r - R_{\text{abs}})^2, \quad (\text{B.5})$$

where  $\theta(x)$  is the Heaviside step function, and the values  $R_{\text{abs}} = 1100$  au and  $c_{\text{abs}} = 5 \times 10^{-5}$  au were used. With this choice of parameters, reflections from both the box boundary and the absorption potential itself are negligible.

To solve (B.3), we use a second-order split-exponential propagator,

$$\Psi(t + dt) = U(t + dt, t) \Psi(t), \quad (\text{B.6a})$$

$$U(t + dt, t) = e^{-i\alpha dt \vec{A}(t + \frac{dt}{2}) \cdot \vec{P}} e^{-i\frac{dt}{2} H_0} e^{-i dt V_{\text{abs}}} e^{-i\frac{dt}{2} H_0}. \quad (\text{B.6b})$$

The initial state  $\Psi_g$  is strongly localized and the propagation starts before the external field is switched on. Therefore, the individual exponential factors on the rhs of (B.6a) can be permuted cyclically without affecting the final result (once a specific ordering is chosen, however, it must be kept across the whole simulation). Since the wave function is represented in the basis of the eigenstates of the field-free Hamiltonian  $H_0$ , the first and third stages of the time-step propagation are trivial. Furthermore, the spectral resolution of the time-independent absorber is known, so the second stage is computationally inexpensive as well. The last stage, which accounts for radiative transitions, requires the evaluation of the action of the exponential of a large matrix (size of the order of  $10^5$ ) on the vector to be propagated. For moderately intense fields, this operation is efficiently accomplished with a Krylov scheme [76] which generally

does not require more than 6–7 iterations to converge. The time-evolution is conducted on a distributed-memory machine using PETSc library [77–79].

To extract the photoelectron distribution  $P_{1s}(E, \hat{\Omega})$  at the end of the simulation, we project the wave-packet on numerically accurate single-ionization multichannel scattering states of the field-free Hamiltonian,  $\psi_{1s, E\hat{\Omega}\sigma}^-$ , fulfilling the incoming boundary conditions,

$$P_{1s}(E, \hat{\Omega}) = \sum_{\sigma} |\langle \psi_{1s, E\hat{\Omega}\sigma}^- | \Psi(t_{\max}) \rangle|^2, \quad (\text{B.7a})$$

$$\langle \Psi_{1s, E\hat{\Omega}\sigma}^- | \Psi_{1s, E'\hat{\Omega}'\sigma'}^- \rangle = \delta_{\sigma\sigma'} \delta(E - E') \delta^{(2)}(\hat{\Omega} - \hat{\Omega}') \quad (\text{B.7b})$$

(see [69] for a thorough comparison of this with other methods to extract asymptotic observables from time-dependent wave-packets). The single-ionization scattering states of helium are obtained with the  $K$ -matrix method [80], an  $L^2$  realization of configuration interaction in the continuum which has been successfully applied to compute photoionization spectra of several atomic and molecular systems [69, 80–86]. The interested reader can find a detailed description of the present implementation of the  $K$ -matrix method in the literature [68, 69, 84, 87].

## References

- [1] Sansone G *et al* 2006 Isolated single-cycle attosecond pulses *Science* **314** 443
- [2] Goulielmakis E *et al* 2008 Single-cycle nonlinear optics *Science* **320** 1614–7
- [3] Paul P M, Toma E S, Breger P, Mullot G, Auge F, Balcou P, Muller H G and Agostini P 2001 Observation of a train of attosecond pulses from high harmonic generation *Science* **292** 1689–92
- [4] Remetter T *et al* 2006 Attosecond electron wave packet interferometry *Nature Phys.* **2** 323
- [5] Krausz F and Ivanov M Yu 2009 Attosecond physics *Rev. Mod. Phys.* **81** 163–234
- [6] Ferrari F, Calegari F, Lucchini M, Vozzi C, Stagira S, Sansone G and Nisoli M 2010 High-energy isolated attosecond pulses generated by above-saturation few-cycle fields *Nature Photon.* **4** 875
- [7] Krause J L, Schafer K J and Kulander K C 1992 High-order harmonic generation from atoms and ions in the high intensity regime *Phys. Rev. Lett.* **68** 3535–8
- [8] L’Huillier A and Balcou P 1993 High-order harmonic generation in rare gases with a 1 ps 1053 nm laser *Phys. Rev. Lett.* **70** 774–7
- [9] Lewenstein M, Balcou P, Ivanov M Yu, L’Huillier A and Corkum P B 1994 Theory of high-harmonic generation by low-frequency laser fields *Phys. Rev. A* **49** 2117
- [10] Sansone G *et al* 2010 Electron localization following attosecond molecular photoionization *Nature* **465** 763
- [11] Schultze M *et al* 2010 Delay in photoemission *Science* **328** 1658
- [12] Kelkensberg F *et al* 2011 Attosecond control in photoionization of hydrogen molecules *Phys. Rev. Lett.* **107** 043002
- [13] Goulielmakis E *et al* 2010 Real-time observation of valence electron motion *Nature* **466** 739–43
- [14] Keldysh L V 1965 Ionization in the field of a strong electromagnetic wave *JETP* **20** 1307–14
- [15] Faisal F H M 1973 Multiple absorption of laser photons by atoms *J. Phys. B: At. Mol. Opt. Phys.* **6** L89
- [16] Reiss H R 1980 Effect of an intense electromagnetic field on a weakly bound system *Phys. Rev. A* **22** 1786
- [17] Lewenstein M, Salieres P and L’Huillier A 1995 Phase of the atomic polarization in high-order harmonic generation *Phys. Rev. A* **52** 4747–54
- [18] Madsen L B 2005 Strong-field approximation in laser-assisted dynamics *Am. J. Phys.* **73** 57
- [19] Vénier V, Taïeb R and Maquet A 1995 Two-color multiphoton ionization of atoms using high-order harmonic radiation *Phys. Rev. Lett.* **74** 4161–4
- [20] Maquet A and Taïeb R 2007 Two-colour IR + XUV spectroscopies: the ‘soft-photon approximation’ *J. Mod. Opt.* **54** 1847–57

- [21] Radcliffe P *et al* 2012 Atomic photoionization in combined intense XUV free-electron and infrared laser fields *New J. Phys.* **14** 043008
- [22] Hentschel M, Kienberger R, Spielmann C, Reider G A, Milosevic N, Brabec T, Heinzmann U, Drescher M and Krausz F 2001 Attosecond metrology *Nature* **414** 509
- [23] Itatani J, Quéré F, Yudin G L, Ivanov M Yu, Krausz F and Corkum P B 2002 Attosecond Streak camera *Phys. Rev. Lett.* **88** 173903
- [24] Kienberger R *et al* 2002 Steering attosecond electron wave packets with light *Science* **297** 1144
- [25] Constant E, Taranukhin V, Stolow A and Corkum P 1997 Methods for the measurement of the duration of high-harmonic pulses *Phys. Rev. A* **56** 3870–8
- [26] Kitzler M, Milosevic N, Scrinzi A, Krausz F and Brabec T 2002 Quantum theory of attosecond XUV pulse measurement by laser dressed photoionization *Phys. Rev. Lett.* **88** 173904
- [27] Kazansky A K and Kabachnik N M 2006 Calculations of the double differential cross section for attosecond laser-assisted photoionization of atoms *J. Phys. B: At. Mol. Opt. Phys.* **39** 5173–86
- [28] Kazansky A K, Sazhina I P and Kabachnik N M 2010 Angle-resolved electron spectra in short-pulse two-color XUV+IR photoionization of atoms *Phys. Rev. A* **82** 033420
- [29] Ge Y 2008 Quantum enhancement in laser-assisted photoionization and a method for the measurement of an attosecond XUV pulse *Phys. Rev. A* **77** 033851
- [30] Vénier V, Taïeb R and Maquet A 1996 Phase dependence of  $(N + 1)$ -color ( $N > 1$ ) IR-UV photoionization of atoms with higher harmonics *Phys. Rev. A* **54** 721–8
- [31] Argenti L and Lindroth E 2010 Ionization branching ratio control with a resonance attosecond clock *Phys. Rev. Lett.* **105** 053002
- [32] López-Martens R, Mauritsson J, Johnsson P, Varjú K, L’Huillier A, Kornelis W, Biegert J, Keller U, Gaarde M B and Schafer K J 2004 Characterization of high-order harmonic radiation on femtosecond and attosecond time scales *Appl. Phys. B* **78** 835–40
- [33] López-Martens R *et al* 2005 Amplitude and phase control of attosecond light pulses *Phys. Rev. Lett.* **94** 033001
- [34] Mauritsson J, Johnsson P, López-Martens R, Varjú K, L’Huillier A, Gaarde M B and Schafer K J 2005 Probing temporal aspects of high-order harmonic pulses via multi-colour, multi-photon ionization processes *J. Phys. B: At. Mol. Opt. Phys.* **38** 2265–78
- [35] Varjú K *et al* 2005 Reconstruction of attosecond pulse trains using an adiabatic phase expansion *Phys. Rev. Lett.* **95** 243901
- [36] Mairesse Y *et al* 2003 Attosecond synchronization of high-harmonic soft x-rays *Science* **302** 1540–3
- [37] Mauritsson J, Dahlström M J, Mansten E and Fordell T 2009 Sub-cycle control of attosecond pulse generation using two-colour laser fields *J. Phys. B: At. Mol. Opt. Phys.* **42** 134003
- [38] Dahlström M J, Huillier L A and Maquet A 2012 Introduction to attosecond delays in photoionization *J. Phys. B: At. Mol. Opt. Phys.* **45** 183001
- [39] Dahlström M J, Guénot D, Klünder K, Gisselbrecht M, Mauritsson J, L’Huillier A, Maquet A, Taïeb R, Huillier A L and Huillier A L 2013 Theory of attosecond delays in laser-assisted photoionization *Chem. Phys.* **414** 53
- [40] Klünder K *et al* 2011 Probing single-photon ionization on the attosecond time scale *Phys. Rev. Lett.* **106** 143002
- [41] Swoboda M, Fordell T, Klünder K, Dahlström M J, Miranda M, Buth C, Schafer K J, Mauritsson J, L’Huillier A and Gisselbrecht M 2010 Phase measurement of resonant two-photon ionization in helium *Phys. Rev. Lett.* **104** 103003
- [42] Haessler S *et al* 2009 Phase-resolved attosecond near-threshold photoionization of molecular nitrogen *Phys. Rev. A* **80** 011404
- [43] Caillat J, Maquet A, Haessler S, Fabre B, Ruchon T, Salières P, Mairesse Y and Taïeb R 2011 Attosecond resolved electron release in two-color near-threshold photoionization of  $N_2$  *Phys. Rev. Lett.* **106** 093002
- [44] Baggesen J C and Madsen L B 2011 Atomic and molecular phases through attosecond streaking *Phys. Rev. A* **83** 021403(R)



- [45] Moore L R, Lysaght M a, Parker J S, van der Hart H W and Taylor K T 2011 Time delay between photoemission from the 2p and 2s subshells of neon *Phys. Rev. A* **84** 061404
- [46] Zhang C and Thumm U 2011 Streaking and Wigner time delays in photoemission from atoms and surfaces *Phys. Rev. A* **84** 033401
- [47] Pazourek R, Feist J, Nagele S and Burgdo J 2012 Attosecond streaking of correlated two-electron transitions in Helium *Phys. Rev. Lett.* **108** 163001
- [48] Nagele S, Pazourek R, Feist J and Burgdörfer J 2012 Time shifts in photoemission from a fully correlated two-electron model system *Phys. Rev. A* **85** 033401
- [49] Ivanov I A and Kheifets A S 2013 Extraction of the attosecond time delay in atomic photoionization using the soft-photon approximation *Phys. Rev. A* **87** 063419
- [50] Kheifets A S 2013 Time delay in valence-shell photoionization of noble-gas atoms *Phys. Rev. A* **87** 063404
- [51] Su J, Ni H, Becker A and Jaro-Becker A 2013 Numerical simulation of time delays in light-induced ionization *Phys. Rev. A* **87** 033420
- [52] Johnsson P *et al* 2005 Attosecond electron wave packet dynamics in strong laser fields *Phys. Rev. Lett.* **95** 013001
- [53] Johnsson P, Mauritsson J, Remetter T, L'Huillier A and Schafer K J 2007 Attosecond control of ionization by wave-packet interference *Phys. Rev. Lett.* **99** 233001
- [54] Ranitovic P, Tong X-M, Hogle C, Zhou X, Liu Y, Toshima N, Murnane M and Kapteyn H 2011 Controlling the XUV transparency of helium using two-pathway quantum interference *Phys. Rev. Lett.* **106** 193008
- [55] Laurent G, Cao W, Li H, Wang Z and Cocke C L 2012 Attosecond control of orbital parity mix interferences and the relative phase of even and odd harmonics in an attosecond pulse train *Phys. Rev. Lett.* **109** 083001
- [56] Faisal F H M 1987 *Theory of Multiphoton Processes* (New York: Plenum)
- [57] Cionga A, Florescu V, Maquet A, Taïeb R and Taieb R 1993 Target dressing effects in laser-assisted x-ray photoionization *Phys. Rev. A* **47** 1830
- [58] Zhang C-H and Thumm U 2010 Electron-ion interaction effects in attosecond time-resolved photoelectron spectra *Phys. Rev. A* **82** 043405
- [59] Abramowitz M and Stegun I A 1965 *Handbook of Mathematical Functions with Formulas, Graphs and Mathematical Tables* (New York: Dover)
- [60] Messiah A 1961 *Quantum Mechanics* (Amsterdam: North-Holland)
- [61] Swoboda M, Dahlström M J, Ruchon T, Mauritsson J and L'Huillier A 2009 Intensity dependence of two-color laser-assisted photoionization spectra *Laser Phys.* **19** 1591
- [62] Varjú K *et al* 2006 Angularly resolved electron wave packet interferences *J. Phys. B: At. Mol. Opt. Phys.* **39** 3983
- [63] Vrakking M J J 2001 An iterative procedure for the inversion of two-dimensional ion/photoelectron imaging experiments *Rev. Sci. Instrum.* **72** 4084–9
- [64] Eppink A T J B and Parker D H 1997 Velocity map imaging of ions and electrons using electrostatic lenses: application in photoelectron and photofragment ion imaging of molecular oxygen *Rev. Sci. Instrum.* **68** 3477–84
- [65] Guyétant O *et al* 2005 Multicolour above-threshold ionization of helium: quantum interference effects in angular distributions *J. Phys. B: At. Mol. Opt. Phys.* **38** L357–63
- [66] Guyétant O *et al* 2008 Evolution of angular distributions in two-colour, few-photon ionization of helium *J. Phys. B: At. Mol. Opt. Phys.* **41** 051002
- [67] Colosimo P *et al* 2008 Scaling strong-field interactions towards the classical limit *Nature Phys.* **4** 386–9
- [68] Lindroth E and Argenti L 2012 Atomic resonance states and their role in charge changing processes *Adv. Quantum Chem.* **63** 247
- [69] Argenti L, Pazourek R, Feist J, Nagele S, Liertzer M, Persson E, Burgdörfer J and Lindroth E 2013 Photoionization of helium by attosecond pulses: extraction of spectra from correlated wave functions *Phys. Rev. A* **87** 053405
- [70] Varshalovich D A, Moskalev A N and Khersonskii V K 1988 *Quantum Theory of Angular Momentum* (Singapore: World Scientific)

- [71] Fiebig H R 1980 A spline function approach to the numerical treatment of scattering and bound-state problems for nonlocal potentials *Comput. Phys. Commun.* **20** 181–9
- [72] Bachau H, Cormier E, Decleva P, Hansen J E and Martín F 2001 Applications of B-splines in atomic and molecular physics *Rep. Prog. Phys.* **64** 1815–943
- [73] Argenti L and Colle R 2009 On the B-splines effective completeness *Comput. Phys. Commun.* **180** 1442
- [74] Carroll D P, Silverstone H J and Metzger R M 1979 Piecewise polynomial configuration interaction natural orbital study of  $1s^2$  Helium *J. Chem. Phys.* **71** 4142–63
- [75] Frankowski K and Pekeris C L 1966 Logarithmic terms in the wave functions of the ground state of two-electron atoms *Phys. Rev.* **146** 46
- [76] Hochbruck M and Lubich C 1997 On krylov subspace approximations to the matrix exponential operator *SIAM J. Numer. Anal.* **34** 1911
- [77] Balay S, Brown J, Buschelman K, Gropp W D, Kaushik D, Knepley M G, McInnes L C, Smith B F and Zhang H 2012 PETSc web page ([www.mcs.anl.gov/petsc](http://www.mcs.anl.gov/petsc))
- [78] Balay S, Brown J, Buschelman K, Eijkhout V, Gropp W D, Kaushik D, Knepley M G, McInnes L C, Smith B F and Zhang H 2012 PETSc users manual *Technical Report* ANL-95/11—Revision 3.3, Argonne National Laboratory
- [79] Balay S, Gropp W D, McInnes L C and Smith B F 1997 Efficient management of parallelism in object oriented numerical software libraries *Modern Software Tools in Scientific Computing* ed E Arge, A M Bruaset and H P Langtangen (Basel: Birkhäuser) pp 163–202
- [80] Cacelli I, Carravetta V, Rizzo A and Moccia R 1991 The calculation of photoionization cross sections of simple polyatomic molecules by  $L^2$  methods *Phys. Rep.* **205** 283
- [81] Cacelli I and Carravetta V 1996 Calculation of the differential photoionization cross section of HF *Chem. Phys.* **204** 89–98
- [82] Fang T and Chang T 2000 B-spline-based multichannel  $K$ -matrix method for atomic photoionization *Phys. Rev. A* **61** 062704
- [83] Cacelli I, Moccia R and Montuoro R 2001 Calculation of the differential photoionization cross-section of formaldehyde *Chem. Phys. Lett.* **347** 261–7
- [84] Argenti L and Moccia R 2006  $K$ -matrix method with B-splines:  $\sigma_n$ ,  $\beta_n$  and resonances in He photoionization below  $N = 4$  threshold *J. Phys. B: At. Mol. Opt. Phys.* **39** 2773
- [85] Argenti L and Moccia R 2008 Helium  $2^3S$  photoionization up to the  $N = 5$  threshold *J. Phys. B: At. Mol. Opt. Phys.* **41** 035002
- [86] Argenti L and Moccia R 2010 Nondipole effects in helium photoionization *J. Phys. B: At. Mol. Opt. Phys.* **43** 235006
- [87] Argenti L and Moccia R 2007  $^3S$ ,  $^3P^{o,e}$ ,  $^3D^{e,o}$  resonance series in Helium *J. Phys. B: At. Mol. Opt. Phys.* **40** 3655